SPITZER 24μm SURVEY FOR DUST DISKS AROUND HOT WHITE DWARFS

You-Hua Chu

Kate Y.L. Su

Jana Bilikova

Robert A. Gruendl

Orsola De Marco

See next page for additional authors

Recommended Citation

Chu, You-Hua .... A. Updike, et al. 2011. "Spitzer 24 m Survey for Dust Disks Around Hot White Dwarfs." *Astronomical Journal* 142: 75.

Authors

You-Hua Chu, Kate Y.L. Su, Jana Bilikova, Robert A. Gruendl, Orsola De Marco, Martin A. Guerrero, Adria Updike, Kevin Volk, and Thomas Rauch

SPITZER 24 μm SURVEY FOR DUST DISKS AROUND HOT WHITE DWARFS

You-Hua Chu (朱有花)[1], Kate Y. L. Su[2], Jana Bilikova[1], Robert A. Gruendl[1], Orsola De Marco[3], Martin A. Guerrero[4], Adria C. Updike[5,6,7], Kevin Volk[8], and Thomas Rauch[9]

[1] Department of Astronomy, University of Illinois at Urbana-Champaign, Urbana, IL 61801, USA; yhchu@illinois.edu
[2] Stewart Observatory, University of Arizona, Tucson, AZ 85721, USA
[3] Department of Physics and Astronomy, Macquarie University, Sydney, NSW 2109, Australia
[4] Instituto de Astrofísica de Andalucía, CSIC, E-18008 Granada, Spain
[5] CRESST and the Observational Cosmology Laboratory, NASA/GSFC, Greenbelt, MD 20771, USA
[6] Department of Astronomy, University of Maryland, College Park, MD 20742, USA
[7] Department of Physics and Astronomy, Clemson University, Clemson, SC 29634-0978, USA
[8] Space Telescope Science Institute, Baltimore, MD 21218, USA
[9] Institut für Astronomie und Astrophysik Tübingen (IAAT), Abteilung Astronomie, D-72076 Tübingen, Germany

ABSTRACT

Two types of dust disks around white dwarfs (WDs) have been reported: small dust disks around cool metal-rich WDs consisting of tidally disrupted asteroids and a large dust disk around the hot central WD of the Helix planetary nebula (PN) possibly produced by collisions among Kuiper-Belt-like objects. To search for more dust disks of the latter type, we have conducted a *Spitzer* MIPS 24 μm survey of 71 hot WDs or pre-WDs, among which 35 are central stars of PNe (CSPNs). Nine of these evolved stars are detected and their 24 μm flux densities are at least two orders of magnitude higher than their expected photospheric emission. Considering the bias against the detection of distant objects, the 24 μm detection rate for the sample is ≳15%. It is striking that seven, or ∼20%, of the WD and pre-WDs in known PNe exhibit 24 μm excesses, while two, or 5%–6%, of the WDs not in PNe show 24 μm excesses and they have the lowest 24 μm flux densities. We have obtained follow-up *Spitzer* Infrared Spectrograph spectra for five objects. Four show clear continuum emission at 24 μm, and one is overwhelmed by a bright neighboring star but still shows a hint of continuum emission. In the cases of WD 0950+139 and CSPN K 1-22, a late-type companion is present, making it difficult to determine whether the excess 24 μm emission is associated with the WD or its red companion. High-resolution images in the mid-infrared are needed to establish unambiguously the stars responsible for the 24 μm excesses.

Key words: circumstellar matter – infrared: stars – planetary nebulae: general – white dwarfs

Online-only material: color figure

1. INTRODUCTION

The *Spitzer Space Telescope* (Werner et al. 2004), with its superb sensitivity and resolution at infrared (IR) wavelengths, provides an excellent opportunity to study planetary debris disks around stars (Su et al. 2006; Trilling et al. 2008; Carpenter et al. 2009). For instance, a comprehensive *Spitzer* 24 μm survey of main-sequence A-type stars has shown that up to ∼50% of young (≲30 Myr) stars have little or no 24 μm excess emission from debris disks, large debris-disk excesses decrease significantly at ages of ∼150 Myr, and much of the dust detected may be generated episodically by collisions of large planetesimals (Rieke et al. 2005). The dust in these debris disks would have dissipated long before the stars evolve off the main sequence.

Dust can be replenished during late evolutionary stages. As a low- or intermediate-mass star loses a significant fraction of its initial mass to become a white dwarf (WD), its planetary system expands. Sub-planetary objects, such as asteroids and comets, can be injected into very small radii and be tidally pulverized by the WD, while orbital resonances with giant planets can raise the collision rates among sub-planetary objects and generate dust (Debes & Sigurdsson 2002). This freshly produced dust can be detected through IR excesses and allows us to peer into the late evolution of planetary systems.

The first two WDs reported to possess dust disks were G29-38 and GD 362, both exhibiting near-IR excesses that were confirmed spectroscopically to be dust continuum emission (Zuckerman & Becklin 1987; Becklin et al. 2005; Kilic et al.

2005; Reach et al. 2005). A subsequent *Spitzer* survey of 124 WDs at 4.5 and 8.0 μm found one additional dust disk, around WD 2115−560 (Mullally et al. 2007; von Hippel et al. 2007). As G29-38, GD 362, and WD 2115−560 are WDs with photospheric absorption lines of heavy elements, searches for dust disks have been conducted for DAZ and DBZ WDs, and indeed many more dust disks were discovered. For example, a near-IR spectroscopic survey of 20 DAZ WDs found a dust disk around GD 56 (Kilic et al. 2006), the presence of a dust disk around the DAZ WD 1150−153 was diagnosed by *K*-band excess and confirmed spectroscopically (Kilic & Redfield 2007), and *Spitzer* photometric observations of nine DAZ/DBZ WDs revealed dust disks around GD 40, GD 133, and PG 1015+161 (Jura et al. 2007). One common characteristic of these dust disks around DAZ/DBZ WDs is that they are all small, with outer radii ≪0.01 AU. As the dust disks are completely within the Roche limits of the WDs and the dust mass is estimated to be only ∼10^{18} g, it is suggested that tidally disrupted asteroids produce the dust disks and that the accretion of this dust enriches refractory metals, such as Ca, Mg, Fe, and Ti, in the WD atmospheres (Jura 2003; Jura et al. 2007; Zuckerman et al. 2007). To date, ∼20 dust disks around DAZ/DBZ WDs have been reported, all consistent with this suggested origin of tidal disruption of asteroids (Farihi et al. 2010). More dust disks of this type are being found from the *Wide-Field Infrared Survey Explorer* observations of WDs (e.g., Debes et al. 2011).

An entirely different kind of dust disk has been discovered around the central WD of the Helix planetary nebula (PN), WD 2226−210 (Su et al. 2007). *Spitzer* observations of the

Helix Nebula show a bright compact source coincident with the central WD in the 24 and 70 μm bands, and follow-up Infrared Spectrograph (IRS; Houck et al. 2004) observations have verified that the mid-IR emission originates from a dust continuum. The spectral energy distribution (SED) of this IR emitter indicates a blackbody temperature of 90–130 K, and its luminosity, $(5–11) \times 10^{31}$ erg s^{-1}, requires an emitting area of 3.8–38 AU^2. These properties can only be explained by the presence of a dust cloud; furthermore, little extinction exists toward the WD, so the dust cloud must be flattened with a disk geometry. Adopting a stellar effective temperature of 110,000 K for WD 2226$-$210 (Napiwotzki 1999) and assuming astronomical silicates with a power-law size distribution and a maximum grain radius of 1000 μm for the dust grains, models of the SED indicate that the dust disk extends between 35 and 150 AU from the WD and has a mass of $\sim$0.13 $M_\oplus$. Since this dust must have been generated recently and since the radial location of the dust disk corresponds to that of the Kuiper Belt in the solar system, Su et al. (2007) suggest that the dust disk around WD 2226$-$210 was produced by collisions of Kuiper-Belt-like objects (KBOs) or the breakup of comets.

To simulate the dust disk of WD 2226$-$210, the dynamic evolution of a debris disk around a 3 $M_\odot$ star has been modeled from the main sequence (corresponding to $\sim$A0 V) to the WD stage, and it is found that collisions among KBOs may produce the amount of dust observed (Bonsor & Wyatt 2010; Dong et al. 2010). If the dusk disk around the Helix central star is indeed produced by collisions of KBOs, similar dust disks should be found around other WDs and a survey would allow us to assess their frequency of occurrence and physical properties. These results can then be compared with models of debris disks evolution (Bonsor & Wyatt 2010; Dong et al. 2010) for implications on their planetary systems.

To search for dust disks similar to that around the central WD of the Helix Nebula, we have conducted three surveys using *Spitzer* observations: (1) 24 μm survey of hot WDs and pre-WDs (this paper), (2) archival survey of IR excesses of WDs (Chu et al. 2011; A. Riddle et al. 2011, in preparation), and (3) archival survey of IR excesses of central stars of PNe (CSPNs; Bilikova et al. 2011). The combined results from these three surveys will provide a comprehensive picture of post-main-sequence dust production and dynamic evolution of debris disks. This paper reports the results of the *Spitzer* 24 μm survey of hot WDs as well as follow-up spectroscopic and imaging observations for a subset of hot WDs with 24 μm excesses. Section 2 describes the target selection and observations, Section 3 reports the results, and Section 4 discusses the implications. A summary is given in Section 5.

2. OBSERVATIONS AND DATA REDUCTION

The large dust disk around the central WD of the Helix Nebula is detectable at 24 μm because WD 2226$-$210 has a high temperature and thus high luminosity. Stellar luminosity is a steeper function of temperature than of radius, and WDs span a small range of radii; furthermore, stellar effective temperatures are more readily available in the literature than distances and luminosities. Therefore, we use stellar effective temperature as our main target selection criterion and selected targets from two sources for our 24 μm survey. First, we use the Web version of the McCook & Sion (1999) WD Catalog to search for WDs whose spectral classifications indicate temperatures near or higher than 100,000 K; 58 such hot WDs are found. Hot WDs are the youngest WDs and often surrounded by evolved PNe; 22

of the 58 WDs selected are in known PNe. To probe whether or not dust disks are present around pre-WDs, we have selected 14 hot CSPNs (Napiwotzki 1999) whose effective temperatures are $\geqslant$100,000 K but whose surface gravity is not yet high enough to be classified as WDs. Although pre-WDs evolve along tracks of almost constant luminosities in the H-R diagram, we do not select CSPNs with lower effective temperatures as they are usually surrounded by smaller and brighter PNe, making it difficult to obtain accurate photometric measurements of the CSPNs. These 58 WDs and 14 pre-WDs form the target list of our *Spitzer* 24 μm survey for dust disks.

Among the 72 targets, "WD 0123$-$842" was a misnomer from wrong coordinates and has been removed from the Web version of the McCook & Sion WD Catalog (E. Sion 2010, private communication); thus, this spurious object will not be discussed further in this paper. The 71 valid targets are listed in Table 1. The coordinates in Columns 2 and 3 are measured from the Digitized Sky Survey 2 (DSS2), and in many cases represent an improved accuracy when compared with those given by McCook & Sion or SIM-BAD. Unless noted, the effective temperatures ($T_{\rm eff}$) in Column 4 are taken from Napiwotzki (1999) or converted from the spectral classification in Column 5 taken from McCook & Sion's WD catalog. The common name and Galactic PN (PNG) number of associated PNe are given in Columns 6 and 7.

The *Spitzer* observations reported in this paper were obtained from three programs. The main program is our 24 μm survey of the hot WDs or pre-WDs (Program 40953) using MIPS (Rieke et al. 2004). To assess the nature of hot WDs' 24 μm excesses, we have further obtained *Spitzer* IRS, IRAC (Fazio et al. 2004), and MIPS 70 μm observations (Program 50629). As the MIPS 24 μm survey was not completed before the proposal deadline for *Spitzer* Cycle 5, the last cryogenic cycle of the *Spitzer* mission, IRS and MIPS 70 μm observations were obtained for only a subset of hot WDs with 24 μm excesses: CSPN K 1-22, WD 0103+732 (CSPN EGB 1), WD 0127+581 (CSPN Sh 2-188), and WD 0439+466 (CSPN Sh 2-216). Among these four targets, archival IRAC observations are available for WD 0439+466; we have thus obtained new IRAC observations for only the other three. Finally, we have obtained a MIPS 70 μm observation of KPD 0005+5106 (= WD 0005+511) through a *Chandra X-ray Observatory* observing program (GO8-9026). This MIPS observation was merged with our *Spitzer* Program 40953 for convenience.

2.1. MIPS Observations

2.1.1. MIPS 24 μm Observations

In the MIPS 24 μm survey of hot WDs, each of the 71 objects in Table 1 was imaged using the small-field photometry mode which obtained a sequence of 14 dithered exposures in a preset pattern (see the *Spitzer Space Telescope* Observer's Manual for more details). The observations used an exposure time of 10 s and cycled through the pattern three times, yielding a total exposure time of 420 s in the central $3\rlap{.}'2 \times 3\rlap{.}'2$ region. In a typical median background condition, the depth of the survey will reach a 1σ point-source sensitivity of 33.6 μJy. The raw data were processed using the Data Analysis Tool (DAT; Gordon et al. 2005) for basic reduction (e.g., dark subtraction and flat fielding). All individual exposures were first corrected with a scan-mirror-dependent flat to correct for the dark spots due to particulate matter on the pick-off mirror. For targets

Table 1
Survey Sample of Hot White Dwarfs and Pre-white-dwarfs

Star[a] Name	R.A. (J2000)	Decl. (J2000)	T_{eff} (10^3 K)	WD Type	PN Name	PNG Number
WD 0005+511	00 08 18.11	+51 23 16.9	120	DOQZ.4	. . .	. . .
PG 0038+199	00 41 35.31	+20 09 17.5	115	DO	. . .	. . .
WD 0044−121	00 47 03.31	−11 52 18.9	150	PG1159	NGC 246	118.8−74.7
WD 0103+732	01 07 07.74	+73 33 25.2	150	DA.34	EGB 1	124.0+10.7
WD 0108+100	01 11 06.59	+10 21 38.2	84	DOZ.6	. . .	. . .
WD 0109+111	01 12 23.06	+11 23 36.1	110	DOZ.46	. . .	. . .
WD 0121−756	01 22 52.97	−75 21 13.8	180	PG1159	. . .	. . .
WD 0123−842	01 21 55.0	−84 01 23.0	. . .	PG1159	. . .	. . .
WD 0127+581	01 30 33.22	+58 24 50.7	102	DAO.49	Sh 2-188	128.0−04.1
WD 0130−196	01 32 39.31	−19 21 40.4	100	PG1159.5	. . .	. . .
WD 0237+241	02 40 28.47	+24 22 10.4	100	DA0.5	. . .	. . .
IC 289	03 10 19.36	+61 19 00.5	100	. . .	IC 289	138.8+02.8
WD 0316+002	03 18 58.28	+00 23 25.8	100	DA0.5	. . .	. . .
WD 0322+452	03 27 15.42	+45 24 20.2	125	DAO.40	HDW 3	149.4−09.2
NGC 1360	03 33 14.63	−25 52 17.9	110	. . .	NGC 1360	220.3−53.9
WD 0439+466	04 43 21.20	+46 42 06.4	83	DA.61	Sh 2-216	158.5+00.7
WD 0444+049	04 47 04.51	+04 58 41.7	100	DQZO.5	. . .	. . .
WD 0500−156	05 03 07.51	−15 36 22.5	100	DAO.51	A7	215.5−30.8
K 1-27	05 57 02.37	−75 40 21.1	105	. . .	K 1-27	286.8−29.5
WD 0556+106	05 59 24.87	+10 41 39.9	141	DA.36	WeDe 1	197.4−06.4
WD 0615+556	06 19 33.95	+55 36 43.7	94	DAO.54	PuWe 1	158.9+17.8
WD 0615+655	06 20 30.11	+65 34 21.3	100	DA.51	. . .	. . .
A15	06 27 02.04	−25 22 49.3	110	. . .	A15	233.5−16.3
A20	07 22 57.64	+01 45 33.4	119	. . .	A20	214.9+07.8
WD 0726+133	07 29 02.64	+13 14 49.7	130[b]	PG1159	A21	205.1+14.2
NGC 2438	07 41 50.50	−14 44 07.7	114	. . .	NGC 2438	231.8+04.1
WD 0753+535	07 57 51.69	+53 25 17.5	125	DQZO.4	JnEr 1	164.8+31.1
WD 0823+316	08 27 05.57	+31 30 08.2	100	DA0.5	. . .	. . .
NGC 2610	08 33 23.37	−16 08 57.6	100	. . .	NGC 2610	239.6+13.9
WD 0915+201	09 18 33.11	+19 53 08.2	100	DA0.5	. . .	. . .
WD 0939+262	09 42 50.65	+26 01 00.0	100	DA0.5	. . .	. . .
WD 0948+534	09 51 25.98	+53 09 31.0	126	DA.46	. . .	. . .
LSS 1362	09 52 44.50	−46 16 47.1	100	. . .	HeDr 1	273.6+06.1
WD 0950+139	09 52 58.94	+13 44 34.9	110	DA.46	EGB 6	221.5+46.3
WD 1003−441	10 05 45.79	−44 21 33.4	120	PG1159	Lo 4	274.3+09.1
WD 1034+001	10 37 03.81	−00 08 19.6	100	DOZ.5	. . .	. . .
WD 1111+552	11 14 47.72	+55 01 08.3	94	DAO.54	NGC 3587	148.4+57.0
K 1-22	11 26 43.78	−34 22 11.5	141	. . .	K 1-22	283.6+25.3
WD 1144+004	11 46 35.21	+00 12 33.1	150	DO.34	. . .	. . .
LoTr 4	11 52 29.22	−42 17 38.6	120	. . .	LoTr 4	291.4+19.2
BlDz 1	11 53 06.71	−50 50 57.1	128	. . .	BlDz 1	293.6+10.9
BE UMa	11 57 44.84	+48 56 17.9	105	. . .	BE UMa	144.8+65.8
WD 1159−034	12 01 45.97	−03 45 41.3	140	DQZO.4	. . .	. . .
WD 1253+378	12 55 14.77	+37 32 29.7	100	DA.5	. . .	. . .
MeWe 1-3	13 28 04.90	−54 41 58.4	100	. . .	MeWe 1-3	308.2+07.7
WD 1342+443	13 44 26.87	+44 08 33.3	79	DA.7	. . .	. . .
WD 1424+534	14 25 55.40	+53 15 25.2	110	PG1159.46	. . .	. . .
WD 1501+664	15 02 09.94	+66 12 19.6	170	DZQ.3	. . .	. . .
WD 1517+740	15 16 46.23	+73 52 07.0	110	DO.5	. . .	. . .
WD 1520+525	15 21 46.56	+52 22 03.6	150	PG1159.3	JavdSt 1	085.4+52.3
WD 1522+662	15 22 56.70	+66 04 41.5	140	DO	. . .	. . .
WD 1532+033	15 35 09.85	+03 11 16.0	100	DA.5	. . .	. . .
WD 1547+015	15 49 44.98	+01 25 54.6	100	DA.5	. . .	. . .
WD 1622+323	16 24 49.05	+32 17 02.0	78	DA.65	. . .	. . .
WD 1625+280	16 27 33.73	+27 54 33.6	117	DAO.43	A39	047.0+42.4
WD 1707+427	17 08 47.75	+42 41 00.4	100	DOZ.5	. . .	. . .
WD 1729+583	17 29 50.37	+58 18 09.0	84	DA0.6	. . .	. . .
WD 1738+669	17 38 02.60	+66 53 47.7	95	DA.53	. . .	. . .
WD 1749+717	17 49 04.50	+71 45 08.9	100	DAO.5	. . .	. . .
WD 1751+106	17 53 32.27	+10 37 23.7	117	PG1159	A43	036.0+17.6
HaTr 7	17 54 09.30	−60 49 57.1	100	. . .	HaTr 7	332.5−16.9
WD 1827+778	18 25 08.72	+77 55 37.1	76	DA.68	. . .	. . .
WD 1830+721	18 30 04.90	+72 11 34.5	100	DO.5	. . .	. . .
WD 1851−088	18 54 37.18	−08 49 38.8	90	DAO.56	IC 1295	025.4−04.7
WD 1917+461	19 19 10.21	+46 14 51.2	88	DAO.57	A61	077.6+14.7

Table 1
(Continued)

Star[a] Name	R.A. (J2000)	Decl. (J2000)	T_{eff} (10^3 K)	WD Type	PN Name	PNG Number
WD 1958+015	20 00 39.25	+01 43 40.6	. . .	PG1159	NGC 6852	042.5−14.5
WD 2114+239	21 16 52.34	+24 08 50.9	108	DAO.47	A74	072.7−17.1
WD 2115+339	21 17 08.30	+34 12 27.3	170	PG1159.3	MWP 1	080.3−10.4
WD 2209+825	22 08 25.54	+82 44 55.3	100	DO	. . .	. . .
WD 2246+066	22 49 25.29	+06 56 45.8	100	DA.51	. . .	. . .
WD 2324+397	23 27 15.97	+40 01 23.4	126	DO.4	. . .	. . .
WD 2333+301	23 35 53.33	+30 28 06.2	170	DOZ.3	Jn 1	104.2−29.6

Notes.

[a] For hot pre-WDs in PNe, the PN names are given.

[b] He II Zanstra temperature from Phillips (2003).

that have no large-scale extended emission (from either the surrounding PNe or the background Galactic cirrus), a second flat field generated from the data itself was applied to correct the possible dark latency and scattered light gradient in order to enhance photometric sensitivity. Details of these processing procedures can be found in Engelbracht et al. (2007). The final mosaics were then constructed with a pixel size of $1\rlap.{''}245$ (half the size of the physical pixel) for photometry measurements. The calibration factor 4.54×10^{-2} MJy sr^{-1} (DN s^{-1})$^{-1}$ was used to convert the instrumental unit to physical units (Engelbracht et al. 2007).

All final mosaics were astrometrically calibrated by comparisons with the Two Micron All Sky Survey (2MASS; Skrutskie et al. 2006) sources in the field to establish the World Coordinate System (WCS), the accuracy of which is generally better than $\sim 1''$. We first performed source extraction using *StarFinder* (Diolaiti et al. 2000) with a smoothed theoretical point-spread function (PSF) generated by the STinyTim program (Krist 2006). We consider the WD detected if the extracted source position is within $1\rlap.{''}5$ from the given WD position. In other words, this method ensures a point-source-like object is required to be coincident with the given WD position. For sources that are not detected, we estimate their "observed" point-source flux by fixing the PSF at the given WD position on the PSF-subtracted (source-free) image and using the minimum χ^2 technique. In some cases where the nebular emission is bright, this PSF flux is totally dominated by the background (e.g., CSPN IC 289, CSPN MeWe 1-3, and WD 1958+015 in NGC 6852). These PSF fluxes (non-color corrected) are listed in Column 3 of Table 2.

We have estimated the 1σ point-source sensitivity of the observation using the pixel-to-pixel variation inside a radius of $44''$ centered at the source position on the source-free image (i.e., the systematic background noise). The final photometry error includes (1) the systematic error of the observation, estimated from pixel-to-pixel variations; (2) $24\,\mu$m detector repeatability, $\sim 1\%$ of the measured flux; and (3) $24\,\mu$m confusion noise, $\sim 15\,\mu$Jy, a median value estimated from the extragalactic source counts (Dole et al. 2004). These error contributions are summed in quadrature and listed in Column 4 of Table 2 as "uncertainty." This "uncertainty" has no direct relationship to the detectability of the source. It simply reflects the photometric accuracy if a point source was coincident with the given WD position. For non-detections, we also list 3σ upper limits in Column 5 of Table 2, computed as the three times of the uncertainty plus the PSF flux. In most cases, these 3σ upper limits are

totally dominant by the surrounding bright nebular emission as remarked in Column 8 of Table 2.

For detected sources, we have also carried out aperture photometry using a source aperture of $6\rlap.{''}225$ radius, a sky annulus of radii $19\rlap.{''}92$–$29\rlap.{''}88$, and an aperture correction of 1.7. These results are compared with those determined from the PSF-fitting method. When the two measurements for a source are discrepant, we examine the field for nearby objects or background structures that might compromise the photometry, and adopt the measurement that is less compromised. The aperture photometry result is adopted for WD 0439+466, and the PSF-fitting results are adopted for the other eight cases of detections. When IRS observations are available, we use the background-subtracted flux densities near $24\,\mu$m to further constrain the MIPS $24\,\mu$m photometric measurements.

2.1.2. MIPS 70 μm Observations

Four targets were included in the MIPS $70\,\mu$m observations as part of our Program 50629. The three original targets, CSPN K 1-22, WD 0103 + 732, and WD 0439 + 466, were observed in the photometry raster map mode with 3×1 maps in the array column and row direction and a step size of 1/8 array. This yields a uniformly covered area within a diameter of $3\rlap.{'}2$ centered at the target. Each map was repeated four times (cycles) with 10 s integration per frame, resulting in a total effective integration of 960 s. WD 0005+511 was a target from the *Chandra* program GO8-9026. Its $70\,\mu$m observations were made in the default photometry mode, with 10 s integration per frame and three cycles, and the total integration time was 240 s.

The basic reduction (dark subtraction, illumination correction) of the $70\,\mu$m data was processed using DAT, similar to that of the $24\,\mu$m data. The known transient behavior in the $70\,\mu$m array was removed by masking out the sources in the field of view and time filtering the data (Gordon et al. 2007). For the objects in PNe with extended nebulosity seen at $70\,\mu$m, the size of the masked area was adjusted to cover most of the nebulosity accordingly. The final mosaics were combined using the WCS with a subpixel size of $4\rlap.{''}93$. Figure 1 shows the $70\,\mu$m images alongside the $24\,\mu$m images of K 1-22, WD 0103+732, and WD 0439+466.

The $70\,\mu$m image of WD 0103+732 shows bright extended emission with a central peak at the expected WD position. The diffuse emission at $70\,\mu$m, appearing more extended than that in the $24\,\mu$m band, is most likely dominated by bright emission lines such as the [O III] $88\,\mu$m line. To minimize the nebular contamination, we performed aperture photometry with a very

Table 2
MIPS 24 μm Measurements of Hot White Dwarfs and Pre-white-dwarfs

Star Name	MIPS AOR	PSF Flux (mJy)	Uncertainty 1σ (mJy)	Upper Limit 3σ (mJy)	Photometry (mag)	Photospheric (mJy)	Remarks
WD 0005+511	23366144	0.289	0.157	<0.761	$K = 14.19$	0.01164	
PG 0038+199	23366400	0.014	0.050	<0.163	$H = 15.37$	0.00374	
WD 0044−121	23366656	−2.677	9.641	<26.247	$K = 12.87$	0.03925	Very bright nebular emission
WD 0103+732	23366912	2.760	0.141	. . .	$V = 16.35$	0.00058	Superposed on diffuse emission
WD 0108+100	23367168	0.058	0.057	<0.230	$J = 16.33$	0.00130	A point source at 12″ away
WD 0109+111	23367424	0.269	0.055	. . .	$H = 16.05$	0.00200	
WD 0121−756	23367680	0.002	0.038	<0.116	$H = 16.16$	0.00181	
WD 0127+581	23368192	0.338	0.142	. . .	$V = 17.44$	0.00021	Superposed on diffuse emission
WD 0130−196	23368448	0.055	0.049	<0.201	$K = 14.00$	0.01386	
WD 0237+241	23368704	0.073	0.067	<0.274	$J = 16.28$	0.00137	A point source at 9″.5 away
CSPN IC 289	23368960	1210.9	18.2	<1265.6	$K = 15.14$	0.00485	Very bright diffuse emission
WD 0316+002	23369216	−0.026	0.056	<0.142	$z = 19.66$	0.00007	
WD 0322+452	23369472	0.059	0.062	<0.245	$V = 17.20$	0.00026	
CSPN NGC 1360	23369728	−0.605	1.752	<4.651	$K = 12.37$	0.06221	Bright nebular emission
WD 0439+466	23369984	9.200	0.157[a]	. . .	$K = 13.66$	0.01896	Superposed on diffuse emission
WD 0444+049	23370240	−0.003	0.064	<0.187	. . .	. . .	Two sources at 10″–11″ away
WD 0500−156	23370496	0.013	0.047	<0.156	$H = 16.16$	0.00181	
CSPN K 1-27	23370752	11.603	0.372	<12.721	$J = 16.40$	0.00122	Bright nebular emission
WD 0556+106	23371008	0.051	0.071	<0.264	$V = 17.40$	0.00022	A point source at 12″.5 away
WD 0615+556	23371264	0.110	0.049	<0.256	$J = 15.90$	0.00194	Two sources at 3″–4″ away
WD 0615+655	23371520	0.028	0.042	<0.153	$V = 15.70$	0.00105	
CSPN A15	23371776	14.221	0.342	<15.248	$V = 15.72$	0.00103	Very bright nebular emission
CSPN A20	23372032	0.021	2.645	<7.956	$V = 16.56$	0.00048	Very bright nebular emission
WD 0726+133	23372288	0.916	0.114	. . .	$J = 16.58$	0.00104	Superposed on diffuse emission
CSPN NGC 2438	23372544	12.410	13.659	. . .	$J = 17.02$	0.00069	Superposed on diffuse emission
WD 0753+535	23372800	0.197	0.159	<0.675	$J = 16.58$	0.00104	Very bright nebular emission
WD 0823+316	23373056	−0.073	0.055	<0.092	$K = 15.73$	0.00282	
CSPN NGC 2610	23373312	127.5	7.2	<149.0	$H = 16.29$	0.00160	Very bright nebular emission
WD 0915+201	23373568	0.039	0.057	<0.210	$V = 16.64$	0.00044	
WD 0939+262	23373824	−0.008	0.053	<0.151	$H = 15.57$	0.00311	
WD 0948+534	23374080	0.060	0.043	<0.189	$H = 16.15$	0.00183	
CSPN LSS 1362	23374336	−2.934	4.032	<9.164	$K = 12.81$	0.04148	Very bright nebular emission
WD 0950+139	23374592	11.740	0.066	. . .	$K = 16.10$	0.00200	
WD 1003−441	23374848	8.821	3.688	<19.887	$V = 16.60$	0.00046	Very bright nebular emission
WD 1034+001	23375104	0.964	0.133	<1.364	$K = 14.37$	0.00986	Bright nebular emission
WD 1111+552	23375360	2.190	1.320	<6.149	$J = 16.71$	0.00092	Bright nebular emission
CSPN K 1-22	23375616	1.070	0.143	. . .	$K = 14.27$	0.01081	Superposed on diffuse emission
WD 1144+004	23375872	−0.044	0.067	<0.158	$H = 16.13$	0.00186	
CSPN LoTr 4	23376128	32.298	0.359	<33.375	$V = 16.50$[b]	0.00050	Very bright nebular emission
CSPN BlDz 1	23376384	3.746	1.109	<7.073	$V = 18.40$[c]	0.00009	Bright nebular emission
CSPN BE UMa	23376640	0.031	0.045	<0.165	$K = 13.63$	0.01949	
WD 1159−034	23376896	0.044	0.058	<0.218	$K = 15.73$	0.00282	
WD 1253+378	23377152	0.034	0.042	<0.159	$K = 15.45$	0.00365	
CSPN MeWe 1-3	23377408	77.376	0.794	<79.759	. . .	. . .	Very bright nebular emission
WD 1342+443	23377664	0.218	0.041	. . .	$z = 17.56$	0.00049	
WD 1424+534	23377920	0.141	0.044	<0.273	$z = 16.97$	0.00084	A point source 9″ away
WD 1501+664	23378176	0.011	0.038	<0.125	$V = 15.90$	0.00087	A point source 2″ away
WD 1517+740	23378432	0.005	0.038	<0.118	$B = 15.90$	0.00069	
WD 1520+525	23378688	0.232	0.042	<0.358	$J = 16.38$	0.00125	In diffuse 24 μm emission
WD 1522+662	23378944	0.016	0.036	<0.125	$B = 16.40$	0.00043	
WD 1532+033	23379200	0.029	0.050	<0.179	$H = 16.42$	0.00142	
WD 1547+015	23379456	−0.034	0.047	<0.107	$J = 16.43$	0.00119	
WD 1622+323	23379712	0.039	0.038	<0.152	$K = 13.77$	0.01713	
WD 1625+280	23379968	0.093	0.153	<0.553	$J = 16.13$	0.00157	Superposed on diffuse emission
WD 1707+427	23380224	−0.069	0.038	<0.046	$V = 16.70$	0.00042	
WD 1729+583	23380480	−0.025	0.038	<0.090	$z = 19.76$	0.00007	
WD 1738+669	23380736	0.021	0.036	<0.129	$K = 15.45$	0.00365	A point source 12″.5 away
WD 1749+717	23380992	0.004	0.039	<0.123	$J = 16.78$	0.00086	
WD 1751+106	23381248	−1.840	2.641	<6.084	$K = 15.33$	0.00407	Bright nebular emission
CSPN HaTr 7	23381504	0.194	0.294	<1.075	$K = 15.75$	0.00277	Bright nebular emission
WD 1827+778	23381760	0.022	0.037	<0.133	$J = 16.64$	0.00098	A point source 12″.5 away
WD 1830+721	23382016	−0.006	0.040	<0.113	$B = 17.00$	0.00025	A point source 7″ away
WD 1851−088	23382272	5.071	5.496	<21.557	$V = 16.90$[d]	0.00035	Very bright nebular emission
WD 1917+461	23382528	0.049	0.090	<0.318	$V = 17.39$	0.00022	Bright nebular emission

Table 2
(Continued)

Star Name	MIPS AOR	PSF Flux (mJy)	Uncertainty 1σ (mJy)	Upper Limit 3σ (mJy)	Photometry (mag)	Photospheric (mJy)	Remarks
WD 1958+015	23382784	136.0	1.5	<140.4	$V = 17.90$	0.00014	Very bright nebular emission
WD 2114+239	23383040	−0.073	0.061	<0.109	$V = 17.05$	0.00030	
WD 2115+339	23383296	−0.120	0.341	<0.903	$K = 14.18$	0.01174	Bright nebular emission
WD 2209+825	23383552	−0.010	0.040	<0.110	$J = 16.58$	0.00104	
WD 2246+066	23383808	0.067	0.052	<0.222	$B = 16.80^{e}$	0.00030	
WD 2324+397	23384064	0.003	0.075	<0.227	$K = 15.40$	0.00382	Near a patch of diffuse emission
WD 2333+301	23384320	0.363	0.154	<0.824	$J = 16.70$	0.00093	Complex emission, no point source

Notes.
[a] Aperture photometry flux.
[b] From Rauch et al. (1996).
[c] From Rauch et al. (1999).
[d] From Napiwotzki & Schönberner (1995).
[e] From Homeier et al. (1998).

small (16″) aperture and sky annulus of 18″–39″. We have also used PSF fitting to estimate the source brightness. Both methods give a point-source flux of ∼55 mJy. The pixel-to-pixel variations in the data suggest 1σ point-source sensitivity of 8.4 mJy.

WD 0439+466 is coincident with a very faint 70 μm source. The source is superposed on diffuse emission, similar to the case of WD 0103+732. Using the same approach as for WD 0103+732, we estimate the source to have a 70 μm flux density of 9.0 ± 8.4 mJy.

Unlike the above two WDs, CSPN K 1-22 has no obvious source coincident with the WD. The data were very noisy, probably due to many foreground and background sources (evident at 24 μm as well). The estimated 1σ point-source sensitivity is ∼4 mJy. WD 0005+511 is not detected at 70 μm, either; its 1σ sensitivity is 5.4 mJy.

2.2. IRAC Observations

IRAC observations of three targets, CSPN K 1-22, WD 0103 + 732, and WD 0127 + 581, were obtained at 3.6, 4.5, 5.8, and 8.0 μm in our Program 50629. These observations all used a 30 s frame time and a cyclic dither pattern with medium offsets to obtain five frames for a total integration time of 150 s for each target. The basic calibrated data (BCD) frames from these observations were reduced using standard routines within the MOPEX package.

We have measured flux densities in each of the IRAC bands using the IRAF task `phot` to perform aperture photometry. These measurements used a 3″.6 radius source aperture with a background estimated from the surrounding annulus of radii 3″.6–8″.4. An aperture correction based on the results tabulated in the IRAC Data Handbook (ver 3.0) was then applied to obtain the flux densities reported in Table 3.

Archival IRAC observations are available for WD 0439+466 (Program 30432; PI: Burleigh), WD 0726+133 (Program 30285; PI: Fazio), and the CSPN NGC 2438 (Program 68; PI: Fazio). These archival data were downloaded and reduced in the same manner as our own observations. Their flux densities are also reported in Table 3.

2.3. IRS Observations

We have also obtained follow-up IRS observations for CSPN K 1-22, WD 0103+732, WD 0127+581, and WD 0439+466

in our Program 50629. All sources were observed using the low-resolution modules SL1 (7.4–14.5 μm), SL2 (5.2–7.7 μm), LL1 (19.5–38.0 μm), and LL2 (14.0–21.3 μm). See Houck et al. (2004) for a more detailed description of the IRS and its capabilities. CSPN K 1-22 and WD 0103+732 were observed in the IRS staring mode after a peakup on a nearby source. WD 0127+581, the faintest target, was observed in mapping mode where the target was sequentially stepped along the slit to facilitate an improved background subtraction. The SL1 and SL2 observations of WD 0127+581 used 8 pointings spaced by 3″ while the LL1 and LL2 observations used 12 pointings spaced by 6″. The MIPS 24 μm observations of WD 0439+466 showed diffuse emission around the WD, thus the IRS observations of WD 0439+466 were made in the mapping mode to obtain spectra of the WD and the diffuse emission by taking spectra from a series of dense slit positions centered on the WD and sequentially offset in the direction perpendicular to the slit. Specifically, the SL1 and SL2 maps were comprised of nine pointings spaced by 3″.6 while the LL1 and LL2 maps are comprised of five pointings spaced by 10″.6. We summarize the modules, exposure times, and setups used in Table 4.

All spectra were reduced using the CUBISM software (Smith et al. 2007) with the latest pipeline processing of the data and the most recent calibration set (irs_2009_05_20-pb-pfc-trim-omeg-lhllbiasfork.cal). Each low-resolution module contains two sub-slits that are exposed at the same time, e.g., SL1 on source and SL2 off source, and vice versa. We examine the off-source frames, select the ones free of any source contamination, trim the maxima and minima, and use the average to produce a background frame. This two-dimensional background frame is then subtracted from all on-source frames in the corresponding module to remove astrophysical background and to alleviate the bad pixels that contaminate the IRS data. After the two-dimensional background subtraction, we flag the global and record-level bad pixels first using the default CUBISM parameters for automatic bad pixel detection, and then through manual inspection of each BCD record, as well as by backtracking the pixels contributing to a given cube pixel.

The spectra are extracted with aperture sizes large enough to enclose the 24 μm source. See Table 5 for the aperture sizes used for the spectral extractions. For the LL orders, two local background spectra on either side of the source are extracted and averaged for a one-dimensional subtraction of the local background. For the SL orders, a single background spectrum is used for the local one-dimensional background subtraction.
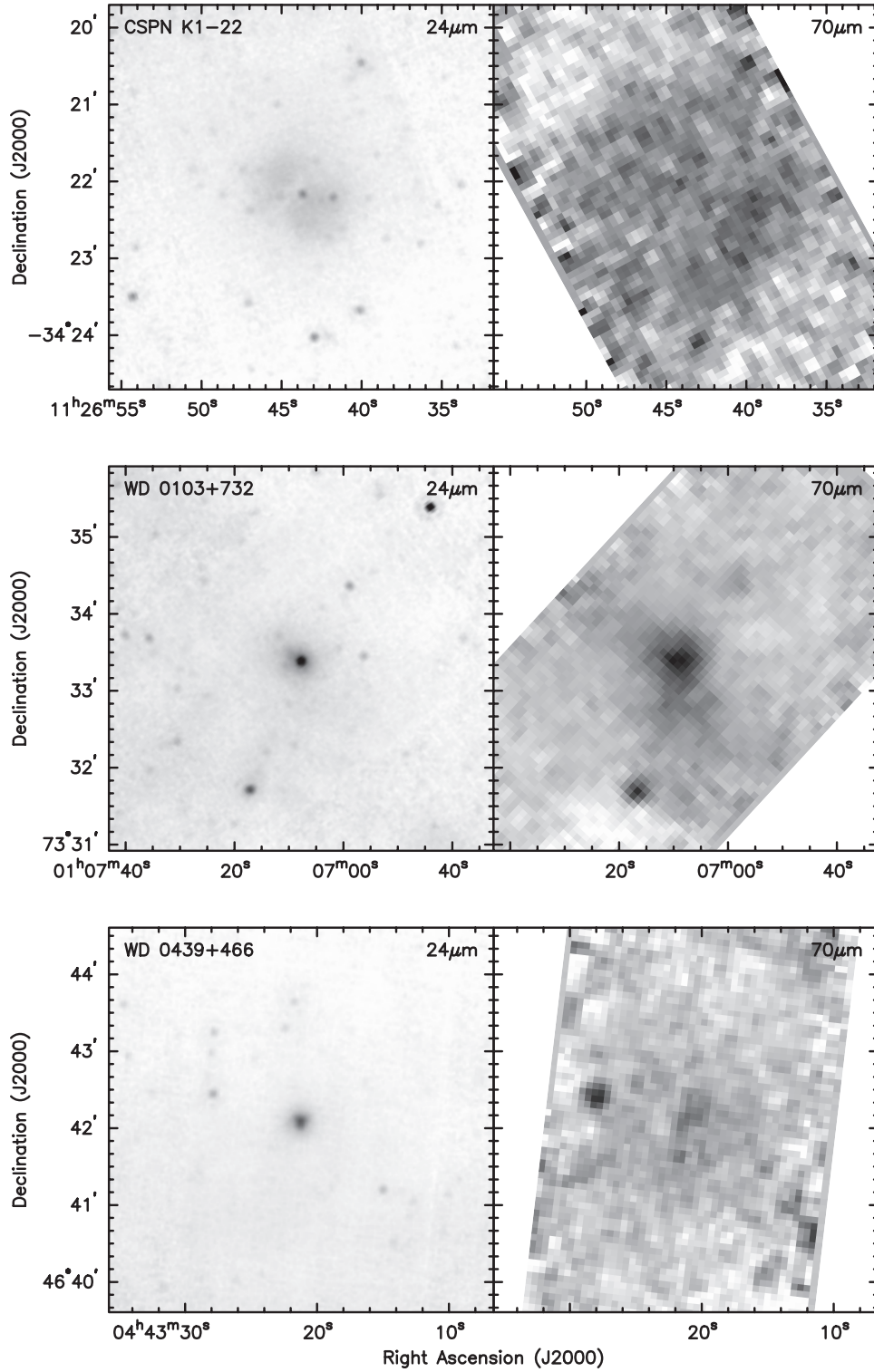
Figure 1. *Spitzer* MIPS 24 and 70 μm images of CSPN K 1-22, WD 0103+732 (CSPN EGB 1), and WD 0439+466 (CSPN Sh 2-216).

Special notes for spectral reduction of individual objects are given below.

WD 0103+732. The frames used for the construction of LL1 background contain a very faint point source. As the WD is bright and the point source is practically removed in the min/max trimming and averaging process, we choose to ignore this faint source so that we can perform the two-dimensional background subtraction to maximize the quality of the final data

cube. In addition, the frames used for the construction of the LL2 background show a small knot of H_2 line emission at 17 μm. This H_2 emission knot is near the center of one slit position, and at the edge of the other slit position. We therefore use only the latter slit position for background subtraction. The pixels of the on-source BCD frames affected by oversubtraction of the emission knot are flagged as record-level bad pixels, and not used for cube construction. Furthermore, this H_2 knot is

Table 3
Spitzer Photometry of Hot White Dwarfs with 24 μm Excesses

WD Name	$f_{3.6\,\mu m}$ (μJy)	$f_{4.5\,\mu m}$ (μJy)	$f_{5.8\,\mu m}$ (μJy)	$f_{8.0\,\mu m}$ (μJy)	$f_{24\,\mu m}$ (μJy)	$f_{70\,\mu m}$ (μJy)
CSPN K 1-22	829 ± 42	706 ± 36	681 ± 38	808 ± 42	1,070 ± 143	<12,000
CSPN NGC 2438	103 ± 40	91 ± 57	82 ± 58	117 ± 95	12,410 ± 13,700[a]	...
WD 0103+732	88 ± 15	71 ± 19	58 ± 20	132 ± 35	2,760 ± 141	<55,000
WD 0109+111	...	...	...	...	269 ± 55	...
WD 0127+581	76 ± 47	56 ± 26	185 ± 161	92 ± 45	338 ± 142	...
WD 0439+466	862 ± 44	514 ± 26	336 ± 22	180 ± 14	9,200 ± 157	9,200 ± 8,400
WD 0726+133	37.7 ± 2.5	22.8 ± 2.0	<19.8	<17.0	916 ± 114	...
WD 0950+139	977 ± 15[b]	1176 ± 15[b]	1773 ± 36[b]	3772 ± 37[b]	11,740 ± 66	...
WD 1342+443	...	...	...	...	218 ± 41	...

Notes.
[a] The photometric uncertainty is dominated by the bright nebular emission.
[b] K. Y. L. Su et al. (2011, in preparation).

Table 4
Summary of the IRS Follow-up Observations

Star Name	Date Observed	IRS Mode	SL1 5.2–8.7 μm	SL2 7.4–14.5 μm	LL1 14.0–21.3 μm	LL2 19.5–38.0 μm
CSPN K1-22	2009 Feb 26	Staring	7 × 60 s	7 × 60 s	8 × 120 s	8 × 120 s
WD 0103+732	2008 Sep 13	Staring	8 × 60 s	8 × 60 s	4 × 120 s	8 × 120 s
WD 0127+581	2008 Oct 9	Mapping[a]	2 × 60 s	2 × 60 s	2 × 120 s	2 × 120 s
WD 0439+466	2008 Sep 7	Mapping[a]	8 × 60 s	16 × 60 s	4 × 120 s	4 × 120 s

Note. [a] Exposure times given are for each pointing in the map.

Table 5
Source and Background Apertures for IRS Spectral Extractions

WD Name	LL1 and LL2 Aperture (arcsec^2)	SL1 and SL2 Aperture (arcsec^2)	LL1 and LL2 Offset (arcsec)	SL1 and SL2 Offset (arcsec)
CSPN K1-22	156	35	20	9.3
WD 0103+732	155	41	20	13.0
WD 0439+466	413	96	25.4	16.7

far enough from the WD position that both a target spectrum and a local background spectrum can be extracted outside the position of the H$_2$ emission knot in the slit. The spectrum of WD 0103+732 is not detected in the SL2 observations.

WD 0127+581. This WD is faint, with $F_{24} = 0.34$ mJy. The orientation of the IRS slit, determined by the roll angle of the spacecraft, was such that a very bright neighboring star was included in the slit. Consequently, the weak emission of WD 0127+581 was overwhelmed by the elevated background from the neighboring star. The spectrum of the WD is not unambiguously detected in the background-subtracted frame; the signal-to-noise ratio (S/N) is too low for meaningful spectral extraction.

WD 0439+466. In its SL2 order, the BCD frames from the three final mapping positions show an abrupt jump in brightness across the center of each frame. Since these slit positions do not contain the target WD, we do not use them for the SL2 cube construction or the SL1 background construction.

3. RESULTS

In our MIPS 24 μm survey of hot WDs, nine of the 71 objects show 24 μm point sources detected at the given WD positions. To assess the physical significance of these 24 μm detections and the 3σ upper limits (see Table 2), we have computed the expected photospheric emission at 24 μm by extrapolating

from the optical and near-IR measurements of each WD. We first searched the Web version of the McCook and Sion WD catalog and the SIMBAD database for available photometric measurements in the *UBVRIJHK* bands and the Sloan Digital Sky Survey (SDSS) *ugriz* bands. For WDs that were discovered from the SDSS (Eisenstein et al. 2006), usually only *ugriz* photometric measurements were available. We also searched the 2MASS Point Source Catalog (Skrutskie et al. 2006) for near-IR counterparts to the WDs. The effective temperatures of our program WDs are so high that it is reasonable to approximate their photospheric emission with a blackbody in the Rayleigh–Jeans limit, i.e., the flux density $F_\nu \propto \nu^2 \propto \lambda^{-2}$. The amounts of extinction to most of these WDs are unknown, but will have smaller impact at longer wavelengths. We thus use the photometric measurement with the longest wavelength and without extinction correction to extrapolate the expected flux density at 23.7 μm, the central wavelength of the MIPS 24 μm band. The fiducial photometric measurement and the expected photospheric emission at 24 μm are given in Columns 6 and 7 of Table 2, respectively.

The expected photospheric emission from these hot WDs are all less than the nominal sensitivity of the 24 μm observations, 0.034 mJy. It is not surprising that all nine detections are at least two orders of magnitude higher than the expected photospheric emission, and thus represent IR excesses. In the cases of non-detections, the 3σ upper limits are several to several tens

times higher than the expected photospheric emission. These non-detections do not exclude the existence of low-level IR excesses, but no useful deductions can be made from these results; thus, the non-detections will not be discussed further in this paper. We have combined all available photometric measurements of the nine WDs and pre-WDs with 24 μm excesses to produce the SEDs plotted in Figure 2. Below we describe individually the nine hot WDs and pre-WDs with 24 μm excesses. Detailed modeling of the SEDs and IRS spectra will be reported by J. Bilikova et al. (2011, in preparation).

3.1. CSPN K 1-22

Multi-wavelength optical and IR images of CSPN K 1-22 are displayed in Figure 3. The DSS2 red image shows a source at 2″ north of the CSPN, but no counterpart of this source is seen in any of the other optical or IR images. It is not clear whether this red source is spurious or transient. The *Hubble Space Telescope* (*HST*) images show two sources separated by 0″.35 at the center of K 1-22; the blue northeast component is the CSPN and the red southwest component is a cool companion (Ciardullo et al. 1999). The IR images show a source coincident with this close pair of stars, but cannot resolve them.

In the SED plot in Figure 2, the flux densities of CSPN K 1-22 and its close companion are individually plotted in the *HST* F555W and F814W bands, while the flux densities in the 2MASS *J H K* and *Spitzer* IRAC and MIPS bands are for the two stars combined. An extinction of $E(B-V) = 0.076$ (Ciardullo et al. 1999) has been corrected from the observed flux densities. The atmospheric emission of the WD has been modeled as a blackbody; for the companion, we adopt the Kurucz atmospheric model for a K2 V star, the spectral type implied by the *HST* photometry. These stellar emission models are plotted in thick solid curves in Figure 2. The IRAC and MIPS flux densities are all higher than the expected atmospheric emission from these two stars. The IR excesses in the near-IR and in the mid-IR cannot be described by a single blackbody; however, two blackbody emitters at temperatures of 700 and 150 K appear to match the IR excesses in the IRAC and MIPS 24 μm bands. The combined SED of the WD, its companion, and the two blackbody emitters is plotted as a thin solid line in Figure 2.

The IRS spectra extracted from CSPN K 1-22 and adjacent background regions all show [Ne III] 15.55 μm, [S III] 18.71 μm, [O IV] 25.89 μm, and [S III] 33.48 μm line emission (see Figure 4). The background-subtracted IRS spectrum of CSPN K 1-22 shows a weak continuum component and residual line emission, especially prominent in the [O IV] line.

To determine the nature of the residual line emission, we compare the spatial distributions of the continuum and line emission. Figure 5 shows the surface brightness profiles along the slit for the 24 μm continuum, [O IV] 25.89 μm line, and [S III] 18.71 μm line, as extracted from the IRS data cube. It is evident that the continuum originates from a point source, the CSPN, while the line emission from the PN is extended. The [S III] line has a lower excitation potential (i.e., ionization potential of s$^+$, 23.3 eV) and shows an extended, nearly flat surface brightness profile; while the [O IV] 25.89 μm line has a higher excitation potential (i.e., ionization potential of O^{+2}, 54.9 eV) and shows a narrower, centrally peaked surface brightness profile. These different spatial distributions are consistent with the expectation from the ionization stratification in a PN.

The MIPS 24 μm image of K 1-22 (Figure 1) shows that the CSPN is superposed on diffuse emission (Chu et al. 2009). The IRS spectra show that this diffuse emission is dominated by the [O IV] 25.89 μm line. The centrally peaked morphology of the diffuse [O IV] emission makes it difficult to subtract the background accurately. As the background spectrum is the average of those extracted from the two regions at ±20″ from the central source, it can be seen from the [O IV] surface brightness profile in Figure 5 that the excess emission at the center is ∼35% of the background emission. The residual [O IV] emission in the background-subtracted spectrum in Figure 4 is indeed about 1/3 as strong as the emission from the background regions. Therefore, the apparent [O IV] emission in the background-subtracted spectrum of CSPN K 1-22 is most likely a residual from imperfect background subtraction.

Figure 4 shows that the MIPS 24 μm band photometric measurement (∼1 mJy) of the CSPN, plotted as an open diamond, appears higher than the continuum flux density of the background-subtracted spectrum (∼0.75 mJy). This discrepancy is likely caused by the contamination of [O IV] line in the MIPS 24 μm band. The photometric measurements in the IRAC 5.8 and 8.0 μm bands, plotted as open diamonds in Figure 4, are also higher than the continuum flux densities; however, these discrepancies are less than 25% and are reasonable for the S/N of the spectrum at these wavelengths.

The background-subtracted IRS spectrum of CSPN K 1-22 shows continuum emission well above the expected photospheric emission of the CSPN and its red companion (∼0.011 mJy), and thus represents an IR excess due to dust continuum. Nevertheless, it is not known whether the excess IR emission is associated with the CSPN or its red companion. High-resolution images in the mid-IR wavelengths are needed to resolve CSPN K 1-22 and its companion.

3.2. CSPN NGC 2438

CSPN NGC 2438 shows bright 24 μm emission more than four orders of magnitude higher than the expected photospheric emission. The MIPS observation of NGC 2438 was made after the *Spitzer* Cycle 5 proposal deadline; thus NGC 2438 was not an IRS target in our Program 50629. However, Bilikova et al. (2009) had found IR excesses of CSPN NGC 2438 through the analysis of archival IRAC observations (see IRAC images in Figure 6) and included NGC 2438 in another *Spitzer* program to study IR excesses of CSPNs (Program 50793; PI: Bilikova). The IRS observations used only the short wavelength modules and therefore only extend to ∼15 μm. The background-subtracted IRS spectrum of the CSPN NGC 2438 exhibits continuum emission (J. Bilikova et al. 2011, in preparation).

The SED of CSPN NGC 2438 (Figure 2) shows that the 24 μm excess is much greater than the IR excesses in the IRAC bands. The IR excesses in the IRAC bands and the MIPS 24 μm band cannot originate from a single-temperature emitter; instead, they can be roughly described by two emitters at 1200 K and 150 K, respectively. Unfortunately, 2MASS did not detect the CSPN NGC 2438 in the *H* and *K* bands to allow a more precise modeling of the SED to determine the temperature of the hotter emitter and whether it originates from a low-mass stellar companion or from a dust disk.

3.3. WD 0103+732 (CSPN EGB 1)

WD 0103+732 is the central star of the PN EGB 1. *HST* images do not show any companion stars (Ciardullo et al. 1999). See Figure 7 for optical, 2MASS *J*, IRAC, and MIPS 24 μm images of WD 0103+732. The SED of WD 0103+732 (Figure 2) shows optical and near-IR flux densities following a blackbody
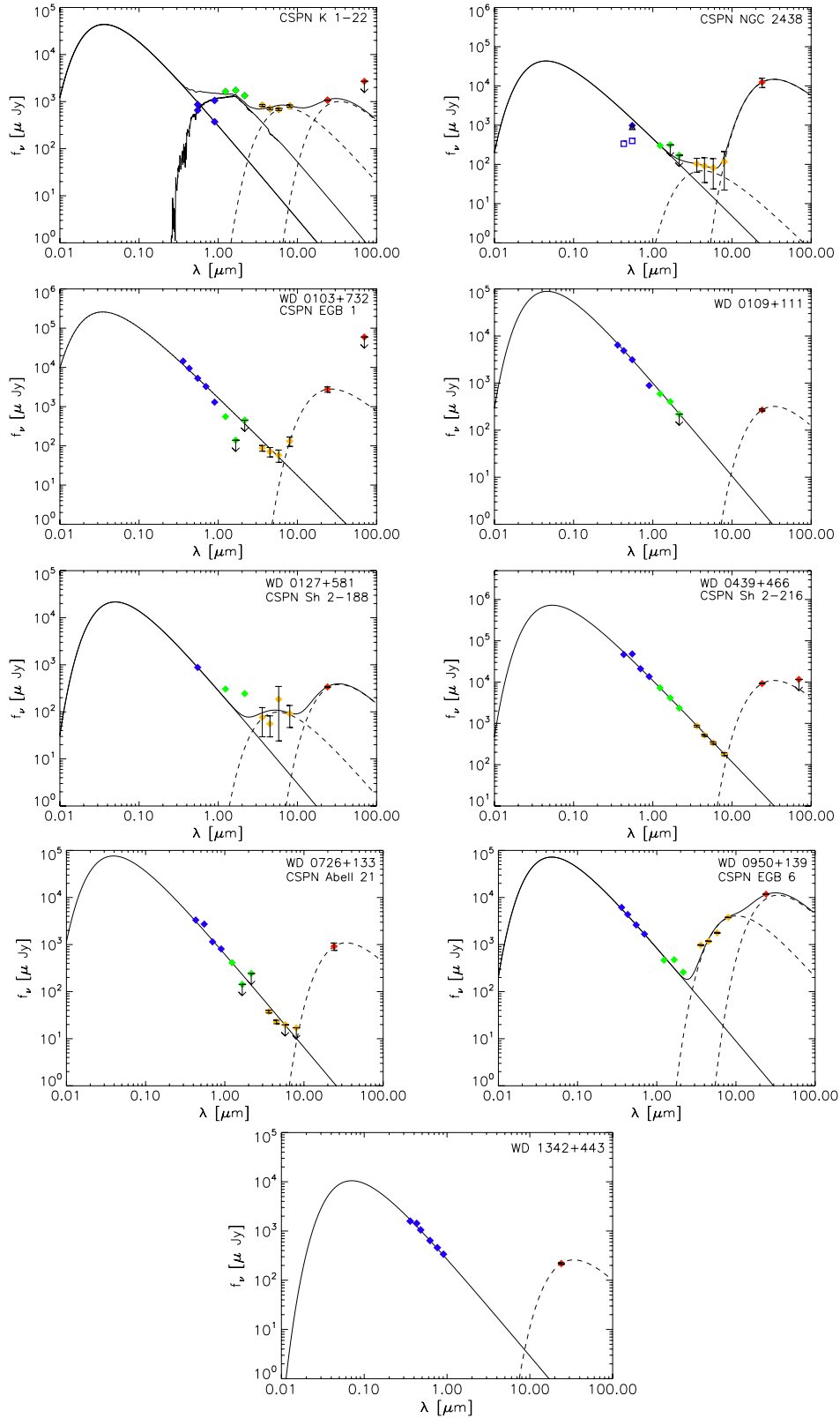
Figure 2. Spectral energy distribution plots for WDs detected in the MIPS 24 μm band. The photometric measurements include published optical magnitudes (blue diamonds), 2MASS JHK (green diamonds), *Spitzer* IRAC bands (yellow diamonds), and MIPS 24 and 70 μm bands (red diamonds). Solid blackbody lines in the optical wavelengths represent the WD photospheric emission, while dashed lines represent the blackbody-like excess emission with the best-fit dust temperatures (see Table 6). For the four objects with excess emission in the IRAC bands, the sum of the stellar emission and two blackbody components is plotted in thin black line.

(A color version of this figure is available in the online journal.)

curve closely, although the WD is not detected in the 2MASS H and K bands, where 2σ upper limits are plotted. The flux density

in the IRAC 8.0 μm band starts to rise above the photospheric emission level, and in the MIPS 24 μm band the flux density is
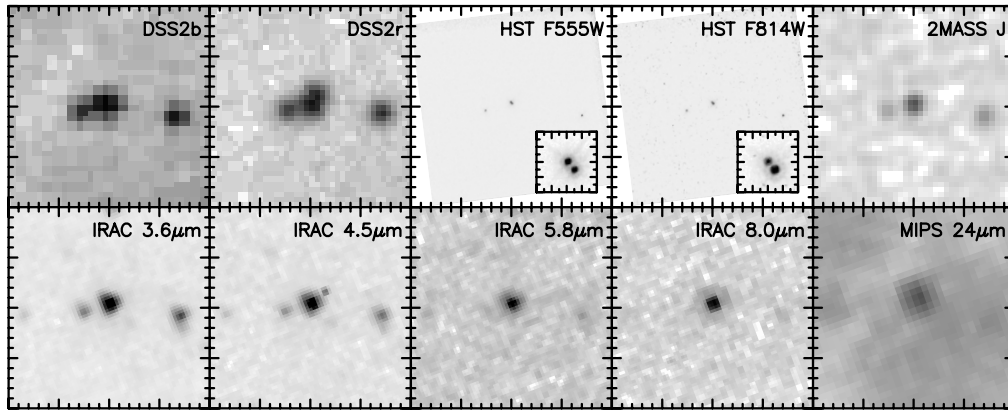
Figure 3. Optical and IR images of CSPN K 1-22. The field of view of each panel is $40'' \times 40''$. The inset in the *HST* images is $2'' \times 2''$.
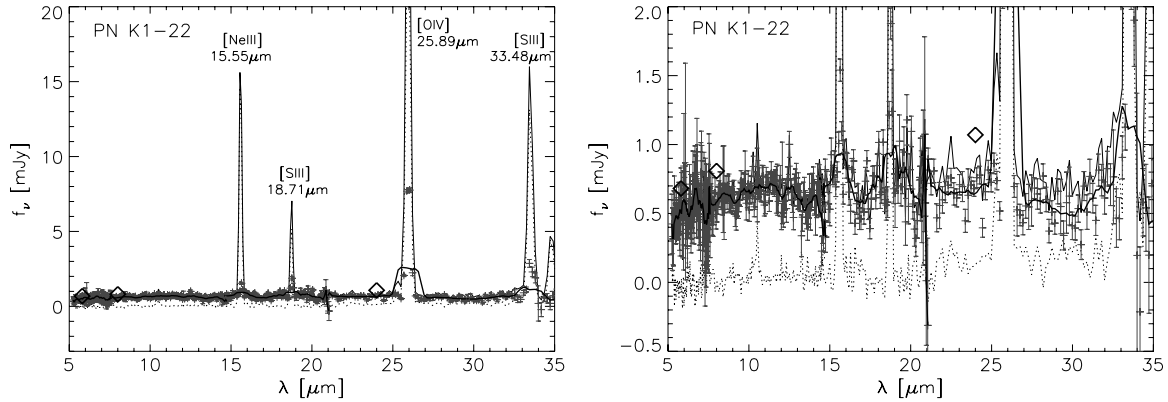
Figure 4. *Spitzer* IRS spectrum of CSPN K 1-22 plotted with different stretches to illustrate the relative intensity of lines and continuum. The spectrum extracted at CSPN K 1-22 is plotted in a thin solid line, the local background spectrum in a dotted line, the background-subtracted spectrum of CSPN K 1-22 in pixels with error bars, and the smoothed background-subtracted spectrum in a thick line.
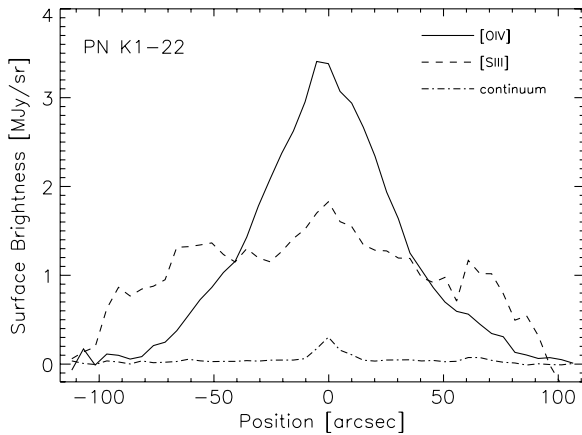
Figure 5. Surface brightness profile plots of CSPN K 1-22 extracted from the *Spitzer* IRS data cube in the continuum (dash-dotted curve), [O IV] 25.89 μm line (solid curve), and [S III] 18.71 μm line (dashed curve).

more than three orders of magnitude higher than expected from photospheric emission.

The MIPS 24 μm image (Figure 1) shows that the point source of WD 0103+732 is superposed on diffuse emission (Chu et al. 2009). The IRS spectrum of the background (see Figure 8) shows that the diffuse emission is dominated by line emission with a weak but appreciable continuum at wavelengths $\gtrsim 20\,\mu$m, and that the major contributor to the MIPS 24 μm emission is the [O IV] 25.89 μm line. The background-subtracted spectrum of

WD 0103+732 (Figure 8) is dominated by continuum emission. The apparent deficit at the [Ne III] and [S III] lines and excess at the [O IV] line are caused by imperfect background subtraction. Figure 9 shows the surface brightness profiles of the 24 μm continuum, [O IV] and [S III] lines extracted from the IRS data cube. The nebular emission near WD 0103+732 also shows ionization/excitation stratification, as the [O IV] emission profile is narrower and more strongly peaked toward the center than [S III], resulting in an undersubtraction of background in the [O IV] line and oversubtractions in the [S III] and [Ne III] lines. Interestingly, the background shows an emission feature at 17 μm, which could be associated with transitions of H_2 or polycyclic aromatic hydrocarbons (PAHs). As the emission feature is narrow and the PAH 11.2 μm feature is not present, we identify this 17 μm feature as the H_2 (0, 0) S(1) line emission. This H_2 emission is associated with a much more extended background and does not vary significantly over the regions of spectral extractions, no residual H_2 17 μm line emission is present in the background-subtracted spectrum of WD 0103+732.

Despite the morphological differences between the PNe EGB1 and the Helix Nebula, the SED and IRS spectrum of WD 0103+732 are very similar to those of WD 2226−210 (Su et al. 2007). Both show IR excess starting in the IRAC 8 μm band and peaking near the MIPS 70 μm band. Because of the bright nebulosity and lower angular resolution of the MIPS 70 μm camera, we consider the 70 μm flux density of WD 0103+732, 55 mJy, an upper limit. As the effective
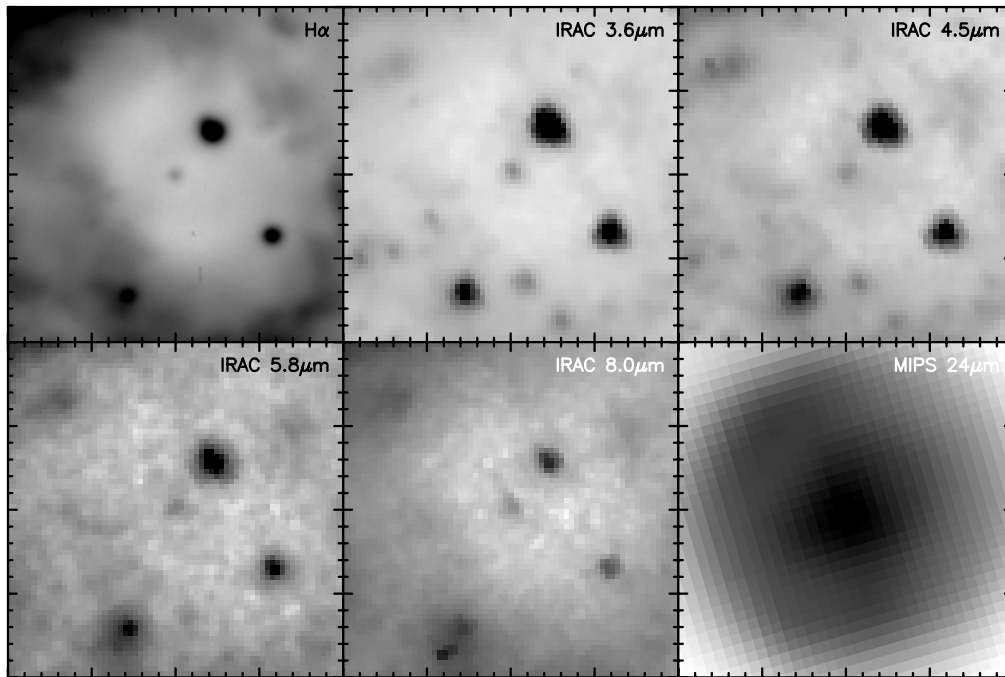
Figure 6. Hα and IR images of NGC 2438. The field of view of each panel is $40'' \times 40''$.
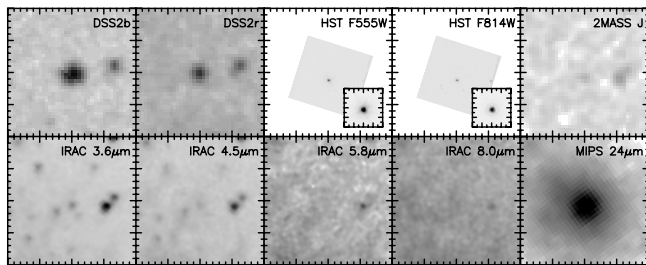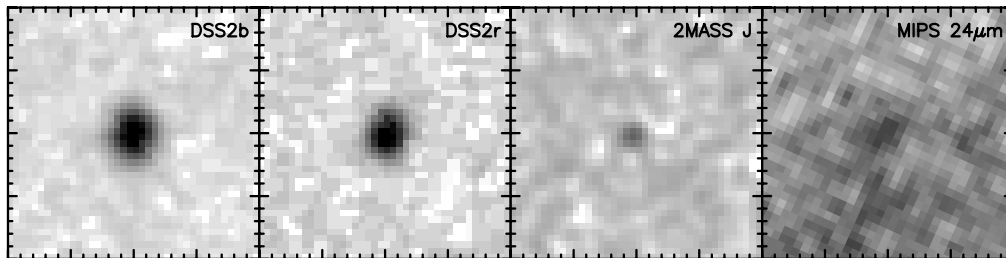

Figure 7. Optical and IR images of WD 0103+732. The field of view of each panel is $40'' \times 40''$. The inset in the *HST* images is $2'' \times 2''$.

temperature of WD 0103+732, ∼150,000 K, is higher than that of WD 2226−210, ∼110,000 K, the physical properties of their dust disks are different (J. Bilikova et al. 2011, in preparation). Note that the light curve of WD 0103+732 shows sinusoidal variations in the *BVR* bands, but the nature of these variations is uncertain (T. Hillwig et al. 2011, in preparation).

3.4. WD 0109+111

This WD is not surrounded by any known PN. It is not in a crowded region. The optical and 2MASS sources are coincident within $1''$; the $24\,\mu m$ source is faint, but also coincident with the optical source within $1''$–$2''$ (see Figure 10). MIPS $24\,\mu m$ images are usually infested with faint background galaxies. We identified ∼20 sources within a $3' \times 3'$ area centered on WD 0109+111. If these sources are randomly distributed within this area, the probability to have one source landing within $2''$ from WD 0109+111 is 4×10^{-4}. Thus, it is unlikely that the $24\,\mu m$ source is a chance superposition of a background source.

The SED of WD 0109+111 (see Figure 2) shows that the optical and near-IR flux densities fall nicely along a blackbody curve, but the $24\,\mu m$ emission is more than 100 times higher than the expected photospheric emission. WD 0109+111 is the
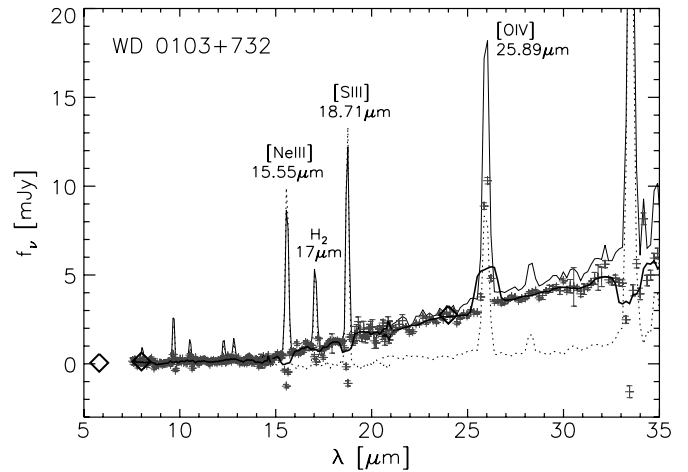
Figure 8. *Spitzer* IRS spectrum of WD 0103+732. The spectrum extracted at WD 0103+732 is plotted in a thin solid line, the local background spectrum in a dotted line, the background-subtracted spectrum of WD 0103+732 in pixels with error bars, and the smoothed background-subtracted spectrum in a thick line.

second faintest $24\,\mu m$ source among the nine detections. No IRS spectra are available for WD 0109+111.

3.5. WD 0127+581 (CSPN Sh 2-188)

WD 0127+581 is surrounded by the PN Sh 2-188. This WD is not detected in the 2MASS *JHK* bands. We have thus used the Kitt Peak National Observatory 2.1 m telescope with the FLAMINGOS detector and measured $J = 17.03 \pm 0.13$ and $K_s = 16.18 \pm 0.13$. We have also obtained IRAC observations of this object. See Figure 11 for these images of WD 0127+581. As WD 0127+581 is a faint source superposed on a bright background, the errors in photometric measurements are large. The WD is easily visible in the 3.6 and $4.5\,\mu m$ bands, but not convincingly detected in the 5.8 and $8.0\,\mu m$
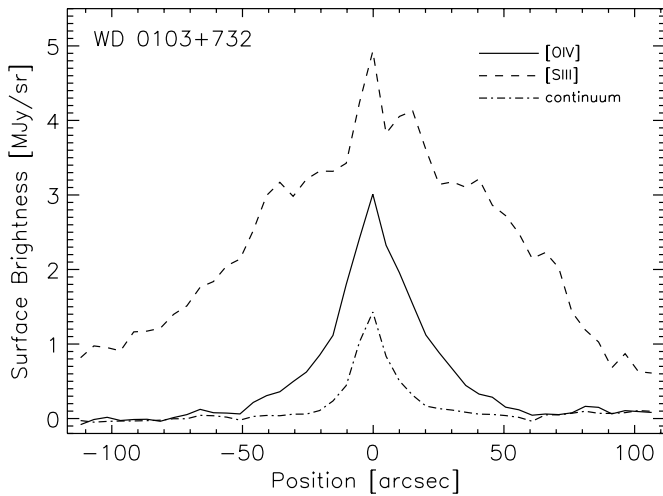
Figure 9. Surface brightness profile plots of WD 0103+732 extracted from the *Spitzer* IRS data cube in the continuum (dash-dotted curve), [O IV] 25.89 μm line (solid curve), and [S III] 18.71 μm line (dashed curve).

bands. As explained in Section 2.3, the weak emission from WD 0127+581 is superposed on an elevated background from a bright neighboring star in the IRS observations. The high noise level prohibits the detection of the spectra of WD 0127+581, and hence no spectra are extracted.

The SED of WD 0127+581 (Figure 2) is complex. The near-IR excess in the *J* and *K* bands is indicative of a late-type companion, while the IR excesses in the IRAC bands and MIPS 24 μm band require two emitters at different temperatures. Two blackbody emitters at temperatures of 900 K and 150 K are plotted in Figure 2 to illustrate one possibility.

3.6. WD 0439+466 (CSPN Sh 2-216)

WD 0439+466 is the central star of the PN Sh 2-216 at a distance of 129 ± 6 pc (Harris et al. 2007). The WD is coincident with a point source surrounded by diffuse emission in the MIPS 24 μm image (Chu et al. 2009). The SED of WD 0439+466 follows the photospheric blackbody curve throughout the optical, 2MASS, and IRAC bands, but shows a large deviation in the MIPS 24 μm band. See Figure 12 for optical and IR images of WD 0439+466.

The IRS spectra of WD 0439+466 and its background are shown in Figure 13. The spectrum of the diffuse emission adjacent to WD 0439+466 shows the [O IV] 25.89 μm and the H$_2$ (0, 0) S(1) 17 μm lines, in addition to a weak continuum that is appreciable at wavelengths greater than $\sim$25 μm. The spectrum extracted at the position of WD 0439+466 also shows the [O IV] and H$_2$ lines, but these emission features are effectively removed by the subtraction of the local nebular background. The background-subtracted spectrum of WD 0439+466 is totally dominated by continuum emission in the 15–35 μm range; furthermore, its flux densities agree well with the photometric measurements in the IRAC 5.8 and 8.0 μm and MIPS 24 μm bands. The continuum-dominated nature of this spectrum is similar to that of the Helix central star. The detailed modeling of WD 0439+466's SED and spectrum will be presented by J. Bilikova et al. (2011, in preparation).

3.7. WD 0726+133 (CSPN A21)

WD 0726+133 is the central star of the PN A21, also known as YM 29. The WD appears as a point source superposed on diffuse emission in the MIPS 24 μm image (Chu et al. 2009). See Figure 14 for optical and IR images of WD 0726+133. The

Figure 10. Optical and IR images of WD 0109+111. The field of view of each panel is $40'' \times 40''$.
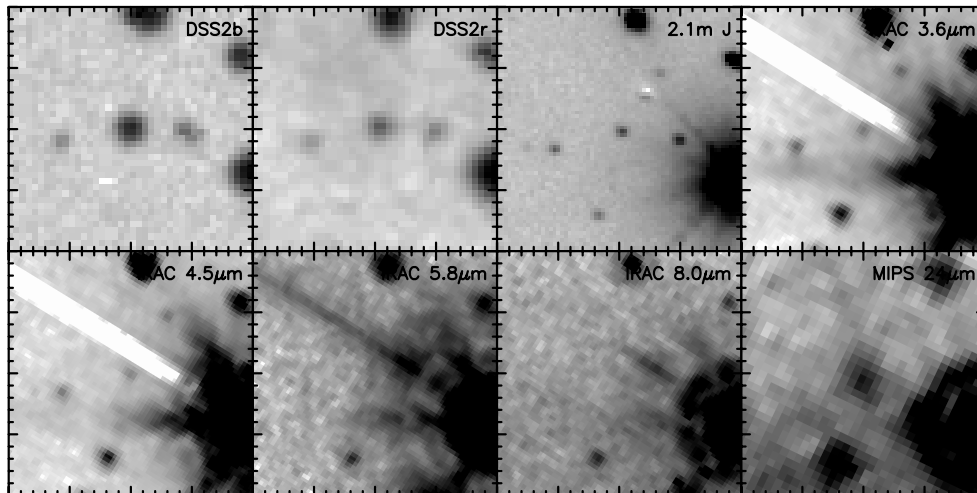

Figure 11. Optical and IR images of WD 0127+581. The field of view of each panel is $40'' \times 40''$.
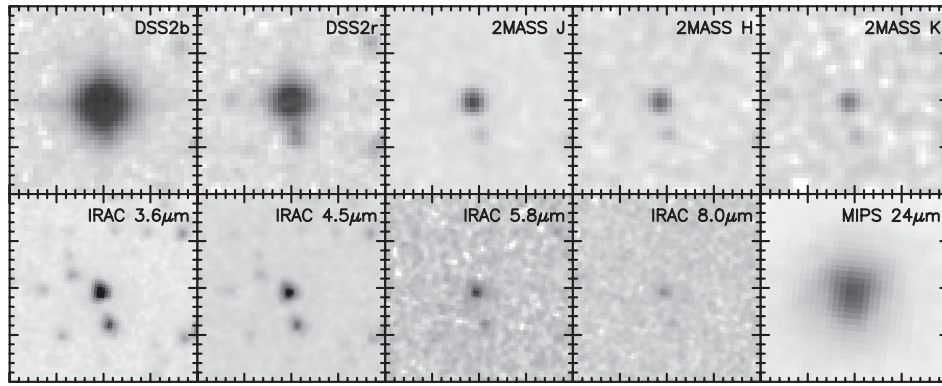
13

Figure 12. Optical and IR images of WD 0439+466. The field of view of each panel is $40'' \times 40''$.
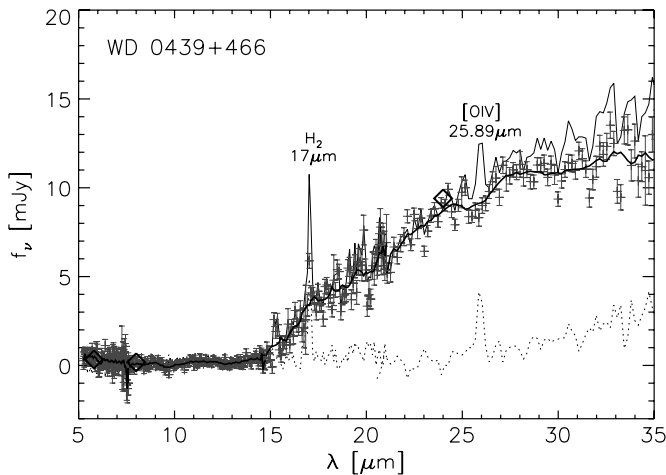

Figure 13. *Spitzer* IRS spectrum of WD 0439+466. The spectrum extracted at WD 0439+466 is plotted in a thin solid line, the local background spectrum in a dotted line, the background-subtracted spectrum of WD 0439+466 in pixels with error bars, and the smoothed background-subtracted spectrum in a thick line.

flux densities of WD 0726+133 in the optical, 2MASS *JHK*, and IRAC bands are all consistent with a blackbody approximation of the stellar photospheric emission. The flux density in the MIPS 24 μm band is almost three orders of magnitude higher than the expected photospheric emission. Several 24 μm sources are detected near WD 0726+133, and their optical counterparts are resolved into spiral galaxies in archival *HST* F555W and F814W images, but WD 0726+133 remains unresolved and shows no companions (Ciardullo et al. 1999). No IRS spectra are available for this WD.

3.8. WD 0950+139 (CSPN EGB 6)

WD 0950+139 is surrounded by the PN EGB 6. This WD previously gained attention because of its strong [O III] and [Ne III] emission lines (Liebert et al. 1989) and near-IR excesses (Fulbright & Liebert 1993). This puzzle was partially solved by an [O III] image taken with the *HST* Faint Object Camera, which revealed an unresolved source $0\farcs18$ from the WD (Bond 1994, 2009). Apparently, WD 0950+139 has a late-type companion and the line emission is associated with the companion. See Figure 15 for optical and IR images of WD 0950+139. Our MIPS 24 μm observation of WD 0950+139 shows a bright unresolved source, and the 24 μm flux density is four orders of magnitude higher than the photospheric emission expected from WD 0950+139 (Figure 2). The SED in the IRAC and

MIPS 24 μm bands cannot be accounted for by a single-temperature emitter; instead, it may be described by two emitters at temperatures of 500 and 150 K. A *Spitzer* IRS spectrum of WD 0950+139 was obtained through Guaranteed Time Observations, and the spectrum confirmed that the emission in the MIPS 24 μm band is dominated by continuum (K. Y. L. Su et al. 2011, in preparation).

3.9. WD 1342+443

This WD was discovered in the SDSS. It is below the detection limit of 2MASS. Figure 16 shows optical and IR images of WD 1342+443. The SED of WD 1342+443 in Figure 2 shows the SDSS photometric measurements falling along the blackbody model curve with the 24 μm flux density more than 400 times higher than the expected photospheric emission. This WD has the faintest 24 μm flux density among the nine hot WDs detected. No IRS spectra are available for WD 1342+443.

4. DISCUSSION

4.1. Statistical Properties

Among our sample of 71 hot WDs, 9 show 24 μm excesses, corresponding to almost 13%. Figure 17 shows the distribution of the sample in *V* and *J*. The number of detections in each magnitude bin is too small to provide meaningful statistics. If the sample is divided into a brighter group that has photometric measurements and a fainter group that has no photometric measurements, it can be seen that 24 μm excesses are detected in 15%–16% of the brighter hot WDs, and only ∼8% among the fainter hot WDs. As all of the WDs in our sample have high temperatures and a small range of radii, their brightnesses are indicative of distances, with the fainter ones being at larger distances. The different percentages of brighter and fainter WDs exhibiting 24 μm excesses most likely reflect the fact that the limiting sensitivity of our MIPS 24 μm survey precludes the detection of distant objects. The true percentage of hot WDs exhibiting 24 μm excesses is likely greater than 15%–16%.

For the nine hot WDs with 24 μm excesses, their 24 μm flux densities are plotted against their *J*-band flux densities in Figure 18. No correlations are seen in this plot. This is expected, as the *J*-band flux density is a rough indicator of distance and the 24 μm excess should not be dependent on distance. Another reason for the lack of correlation is the diverse physical conditions of the 24 μm emitters, as discussed later in Section 4.2.

Seven of the nine hot WDs with 24 μm excesses are still surrounded by PNe: CSPN K 1-22, CSPN NGC 2438,
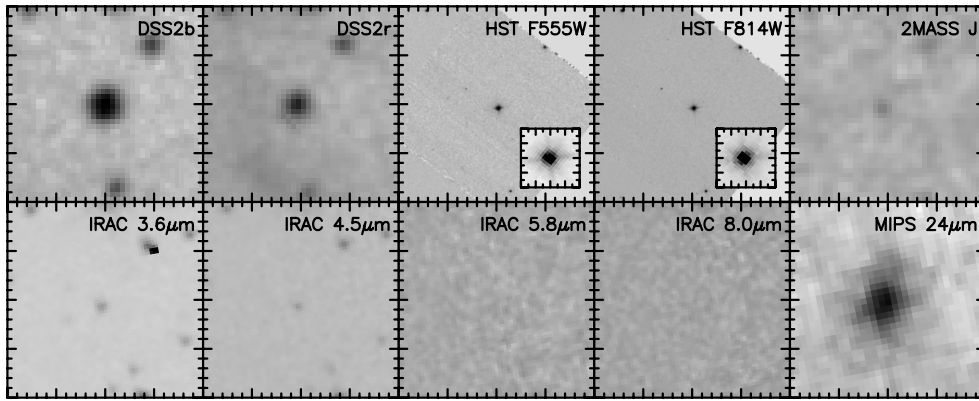
14

Figure 14. Optical and IR images of WD 0726+133. The field of view of each panel is $40'' \times 40''$. The inset in the *HST* images is $2'' \times 2''$.
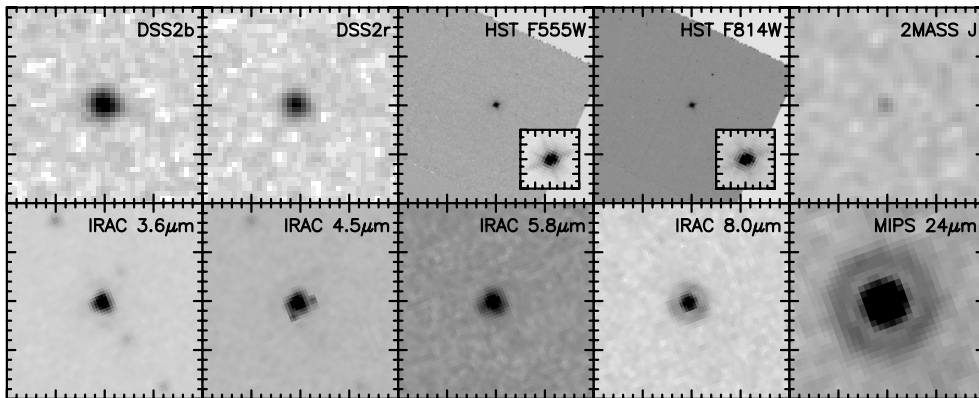

Figure 15. Optical and IR images of WD 0950+139. The field of view of each panel is $40'' \times 40''$. The inset in the *HST* images is $2'' \times 2''$.

WD 0103+732 in EGB 1, WD 0127+581 in Sh 2-188, WD 0439+466 in Sh 2-216, WD 0726+133 in A21 (YM 29), and WD 0950+139 in EGB 6; while two are not in PNe: WD 0109+111 and WD 1342+443. There is a striking difference in the frequency of occurrence of 24 μm excesses between the WDs and pre-WDs in PNe and those without PNe: 20% and 5%–6%, respectively. The two WDs not in known PNe are also the faintest in 24 μm among the nine. WDs without PNe are more evolved than those that are still surrounded by PNe. The smaller 24 μm excesses of the WDs without PNe appear to indicate an evolutionary trend of diminishing excess; however, this trend is not obvious among the 24 μm excesses of the WDs with PNe, if the nebular sizes (Chu et al. 2009) are indicative of their evolutionary status. Considering the diversity in the progenitors' masses and evolutionary paths of these WDs, the current sample of hot WDs with 24 μm excesses is too small to allow us to distinguish between an evolutionary effect and other effects.

4.2. Nature of the 24 μm Excesses

The IR excesses of the CSPN Helix are detected in the 8, 24, and 70 μm bands, but not at shorter wavelengths (Su et al. 2007). High spatial resolution *HST* observation has ruled out any resolved companion earlier than M5 (Ciardullo et al. 1999). Furthermore, the photometric accuracies in the IRAC bands (1σ of 20, 24, 26, and 17 μJy at the 3.6, 4.5, 5.4, and 8.0 μm bands, respectively) can further constrain the mass of a possible companion. At an age of 1 Gyr, the 2MASS and IRAC photometry can also rule out, at the 3σ level, any companion with mass greater than 20 Jupiter masses, i.e., early T dwarfs with $T_{\rm eff} \lesssim 650$ K. Three of the nine new detections of mid-IR excesses of hot WDs show similar SEDs: WD 0103+732

(CSPN EGB 1) shows excess emission at 8 and 24 μm, while WD 0439+466 (CSPN Sh 2-216) and WD 0726+133 (CSPN A21) show excess emission at only 24 μm. Their lack of near-IR excesses does not support the presence of late-type companions.

Four of the hot WDs with 24 μm excesses also exhibit excess emission in the IRAC bands: CSPN K 1-22, CSPN NGC 2438, WD 0127+581 (CSPN Sh 2-188), and WD 0950+139 (CSPN EGB 6). IRS observations indicate that this IR excess is continuum in nature, and crude fits to the SEDs suggest blackbody emitter temperatures of 500–1200 K. These temperatures are in the ranges for brown dwarfs, but the emitting areas, $\sim 1 \times 10^{23}$ to 3×10^{25} cm^2, are too large for brown dwarfs. It is most likely that these IR excesses in the IRAC bands originate from hot dust emission. The two cases with cooler emitter temperatures (500–700 K), CSPN K 1-22 and WD 0950+139, are known to have late-type companions (Ciardullo et al. 1999; Bond 2009). The relationship between these companions and the hot dust components is uncertain. Future searches for companions of CSPN NGC 2438 and WD 0127+581 may help us understand the roles played by stellar companions in producing the dust component responsible for the IRAC excesses. Finally, two hot WDs with 24 μm excesses, WD 0109+111 and WD 1342+443, have no IRAC observations to determine whether excess emission is present in the IRAC bands; their 2MASS measurements do not show any excess emission. In summary, among the 10 hot WDs and pre-WDs that show excess emission at 24 μm, 40% also show near-IR excesses associated with an additional warmer emission component that might be related to the presence of a companion.

Whether a 24 μm excess is accompanied by near-IR excess or not, the shape of the SED suggests that the 24 μm emission
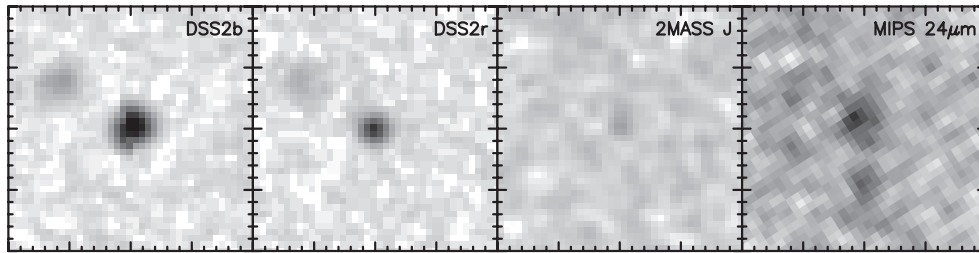
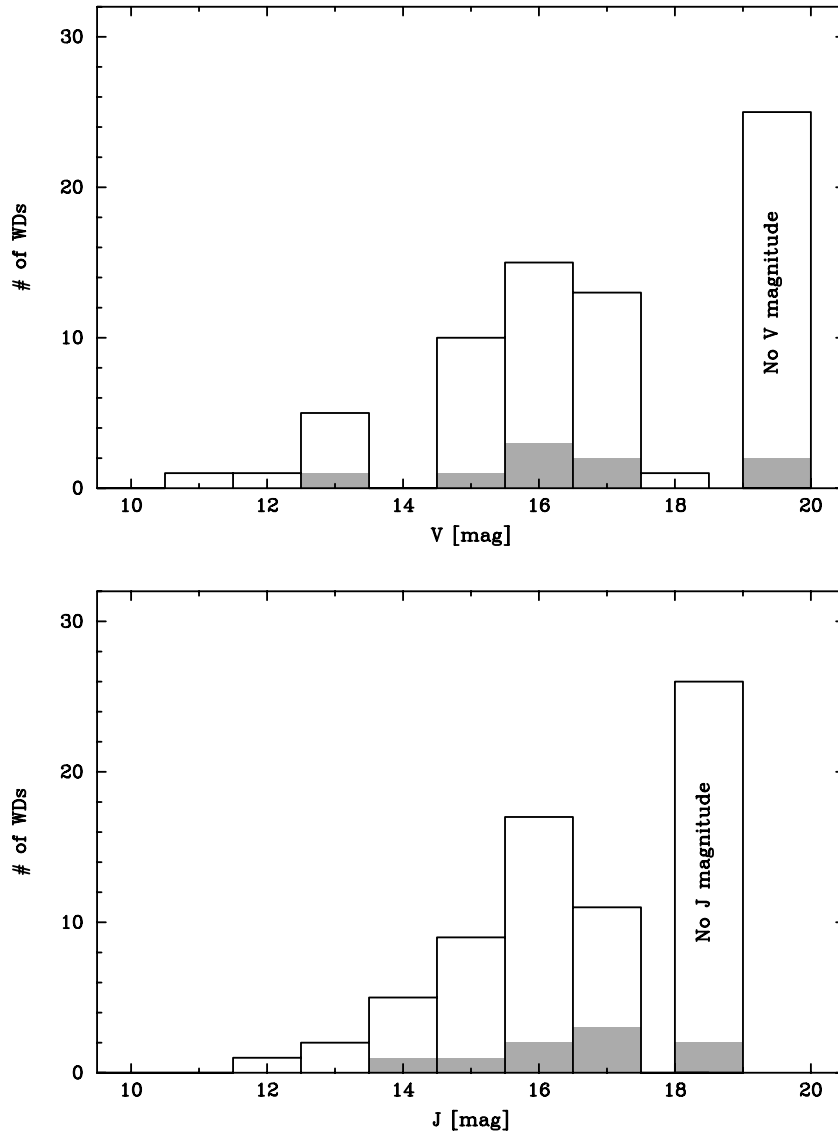**Figure 16.** Optical and IR images of WD 1342+443. The field of view of each panel is $40'' \times 40''$.

Figure 17. Distribution of sample hot WDs in *J* and *V*. The WDs with 24 μm excesses are plotted in shaded boxes.

originates from a component distinct from the WD's photospheric emission or another near-IR emitter. The 24 μm emission must originate from a source cooler than 300 K. Assuming that this source is heated solely by stellar radiation, we can determine the covering factor of the emitter from the luminosity ratio L_{IR}/L_*, where L_{IR} is the luminosity of the excess emitter and L_* is the luminosity of the WD. We adopt the stellar effective temperature, assume a blackbody model, and use the distance and extinction-corrected photometry to determine the stellar luminosity L_*. (Useful physical parameters are listed in Table 6.) The luminosity of the excess emitter is cal-

culated by assuming a 150 K blackbody model normalized at the observed 24 μm flux density. In the case of WD 0103+732 and WD 2226−210, blackbody temperatures are determined from model fits to the 8, 24, and 70 μm flux densities. For the four WDs exhibiting excess emission in the IRAC bands, we add another blackbody component to fit these measurements. These IR emitter models, illustrated in Figure 2, are used to calculate their approximate luminosities. The L_{IR}/L_* ratios of the nine new cases and the Helix CSPN are listed in Table 6. The covering factors range from 4.9×10^{-6} to 4.7×10^{-4}.

Table 6
L_{IR}/L_* of Hot White Dwarfs with 24 μm Excesses

WD Name	Spec Type	T_{eff} (K)	$E(B-V)$	Distance (pc)	R_* ($R_\oplus$)	T_{dust} (K)	L_{IR}/L_*	SED Type[a]	References[b]
CSPN K 1-22	CSPN	141,000	0.076	1,330	3.3	700+150	1.1×10^{-4}	EGB 6-like	1, 2
CSPN NGC 2438	CSPN	114,000	0.25	1,200	4.1	1200+150	4.7×10^{-4}	EGB 6-like	1, 3
WD 0103+732 (CSPN EGB 1)	DA.34	150,000	0.58	650	3.7	190	1.4×10^{-5}	Helix-like	4, 5
WD 0109+111	DOZ.46	110,000	0.065	280	2.3	150	4.9×10^{-6}	Helix-like	6, 7, 8
WD 0127+581 (CSPN Sh 2-188)	DAO.49	102,000	0.27	600	1.7	900+150	6.6×10^{-5}	EGB 6-like	4, 9
WD 0439+466 (CSPN Sh 2-216)	DA.61	83,000	0.065	129	2.4	150	2.4×10^{-5}	Helix-like	10, 11
WD 0726+133 (CSPN A21)	PG1159	130,000	0.13	541	2.0	150	1.6×10^{-5}	Helix-like	2, 11, 12
WD 0950+139 (CSPN EGB 6)	DA.46	110,000	0.21	645	3.0	500+150	4.7×10^{-4}	EGB 6-like	5, 13
WD 1342+443	DA.7	79,000	. . .	437	1.4	150	5.1×10^{-5}	Helix-like	13
WD 2226−210 (CSPN Helix)	DAO.49	110,000	0.03	210	2.6	120	2.5×10^{-4}	Helix-like	11, 14

Notes.
[a] EGB 6-like SEDs show excesses in the IRAC bands as well as the MIPS 24 μm band. Helix-like SEDs show no excess emission at wavelengths shorter than $\sim$8 μm.
[b] References for stellar temperature, extinction, and distance: (1) Rauch et al. 1999, (2) Ciardullo et al. 1999, (3) Phillips 2004, (4) Napiwotzki 2001, (5) Tylenda et al. 1992, (6) Dreizler & Werner 1996, (7) Werner et al. 1997, (8) Wesemael et al. 1985, (9) Kwitter & Jacoby 1989, (10) Rauch et al. 2009, (11) Harris et al. 2007, (12) Phillips 2003, (13) Liebert et al. 2005, and (14) Napiwotzki 1999.
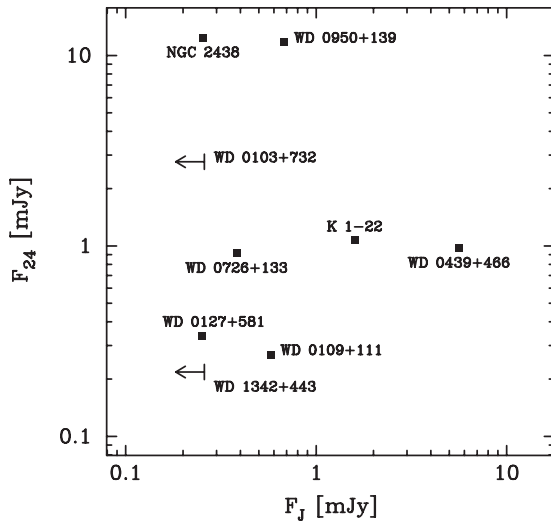

Figure 18. Relationship between F_J and F_{24} for hot WDs showing 24 μm excesses.

A perfect absorbing body heated by a 100,000 K WD to 150 K would be at a distance of $\sim$10 AU, and 100 K at 20 AU. Even at a distance of 10 AU, a covering factor of 4×10^{-6} corresponds to 5×10^{-3} AU^2, or 3×10^6 $R_\odot^2$, too large to be a star or a planet. The most likely origin of this mid-IR emitter is a dust disk, as proposed for the CSPN Helix Nebula (Su et al. 2007). The presence of near-IR excesses indicates the existence of a binary companion or a dust disk at higher temperatures, or both. Detailed modeling and high-resolution images are needed to decipher the true nature of the IR excesses. We defer the modeling of the SEDs and IRS spectra of hot WDs with 24 μm excesses to another paper (J. Bilikova et al. 2011, in preparation).

The connection among CSPNs, circumstellar dust disks, and binarity has been alluded to by various observations and theoretical models. For example, Keplerian circumstellar dust disks have been observed to be associated with binary post-asymptotic giant branch (AGB) stars (de Ruyter et al. 2006). Furthermore, the close binary stellar evolution of CSPNs has been suggested to play a very important role in the formation and shaping of PNe (Soker 1998; Nordhaus & Blackman 2006;

de Marco 2009), although such binary companions are difficult to detect. Our detection of a warmer emitter (500–1200 K) in addition to the colder dust component (at 100–200 K) in four CSPNs, two of which have known companions, appears to further the connection. However, the dust disks responsible for 24 μm excesses are much larger than the circumstellar disks ejected from common-envelope binaries (a few AU at most; Taam & Ricker 2010) and have very different geometry from the Keplerian circumstellar dust disks around binary post-AGB stars, especially in the covering factor (L_{IR}/L_*). The Keplerian circumstellar dust disks around binary post-AGB stars typically have $L_{IR}/L_* \sim$ 0.2–0.5 (de Ruyter et al. 2006), several orders of magnitude higher than those responsible for 24 μm excesses of hot WDs and pre-WDs. This large discrepancy in covering factors suggests that these dust disks have different origins, and the small covering factors are more consistent with debris disks observed in main-sequence stars (Su et al. 2006; Trilling et al. 2008; Wyatt 2008). It is thus likely that the origin of the 24 μm excesses of hot WDs and pre-WDs is dynamically rejuvenated debris disks as suggested by Su et al. (2007).

5. SUMMARY

The central WD of the Helix Nebula has been shown to exhibit excess emission in the *Spitzer* MIPS 24 and 70 μm bands and it is suggested that this IR excess originates from a dust disk produced by collisions among KBOs (Su et al. 2007). Inspired by the WD in the Helix, we have conducted a MIPS 24 μm survey of 71 hot WDs and pre-WDs and found excess 24 μm emission for nine of them. We have further obtained *Spitzer* IRAC and IRS follow-up observations for a subset of these WDs with 24 μm excesses.

The detection of 24 μm excesses is limited by the sensitivity of the observations. Among the hot WDs with optical or near-IR photometric measurements, 15%–16% are detected at 24 μm with excesses. The true occurrence rate of 24 μm excesses must be still higher. Thirty-five of the 71 WDs and pre-WDs in our survey sample are in known PNe; among these 20% show 24 μm excesses, while among the 36 WDs without known PNe only 5%–6% show 24 μm excesses.

The 24 μm excesses are accompanied by different levels of excesses in the *JHK* and IRAC bands. The excess emission in

the *JHK* bands for CSPN K 1-22 and WD 0950+139 (CSPN EGB 6) originates from their known low-mass companions. Excess emission in the IRAC bands are present in CSPN K 1-22, CSPN NGC 2438, WD 0950+139, and WD 0127+581 (CSPN Sh 2-188); IRS spectra show continuum emission clearly in the three former objects and faintly in WD 0127+581, indicating the presence of a dust component at temperatures of $\sim$1000 K. Only WD 0103+732 shows 8, 24, and 70 μm excesses similar to those in the SED of the Helix central WD. In two cases, WD 0439+466 and WD 0726+133, no IR excess is present in the IRAC bands; the IRS spectrum of WD 0439+466 shows that its 24 μm band emission is dominated by dust continuum.

The emitters responsible for the 24 μm excesses have large emitting surface areas that can be provided only by dust disks. Furthermore, the excess emission in these long wavelength bands indicates dust temperatures <300 K. The L_{IR}/L_* ratios of dust disks responsible for the 24 μm excesses of hot WDs and pre-WDs are in the range of 4.9×10^{-6} to 4.7×10^{-4}, similar to those observed in debris disks around main-sequence stars, but several orders of magnitude lower that those of Keplerian circumstellar dust disks around binary post-AGB stars. It is likely that these dust disks around hot WDs and pre-WDs are indeed rejuvenated debris disks as suggested by Su et al. (2007) for the Helix central star.

In two cases, CSPN K 1-22 and WD 0950+139 in EGB 6, late-type companions have been resolved by *HST* images, but *Spitzer* images could not resolve these CSPNs and their companions. It is thus uncertain whether the dust disks are associated with the CSPNs or their companion. High-resolution mid-IR images are needed to establish the associations unambiguously.

REFERENCES

Becklin, E. E., Farihi, J., Jura, M., et al. 2005, ApJ, 632, L119
Bilikova, J., Chu, Y.-H., Gruendl, R., Su, K., & Rauch, T. 2011a, Asymmetric Planetary Nebulae 5 Conference ed. A. A. Zijlstra, F. Lykou, I. McDonald, & E. Lagadec (Manchester: Jodrell Bank Center for Astrophysics)
Bilikova, J., Chu, Y.-H., Su, K., et al. 2009, J. Phys.: Conf. Ser., 172, 012055
Bond, H. E. 1994, in ASP Conf. Ser. 56, Interacting Binary Stars, ed. A. W. Shafter (San Francisco, CA: ASP), 179
Bond, H. E. 2009, J. Phys.: Conf. Ser., 172, 012029
Bonsor, A., & Wyatt, M. 2010, MNRAS, 409, 1631
Carpenter, J. M., Bouwman, J., Mamajek, E. E., et al. 2009, ApJS, 181, 197
Chu, Y.-H., Gruendl, R. A., Bilíková, J., Riddle, A., & Su, K. Y.-L. 2011, in AIP Conf. Proc. 1331, Planetary Systems Beyond the Main Sequence, ed. S. Schuh, H. Drechsel, & U. Heber (Melville, NY: AIP), 230
Chu, Y.-H., Gruendl, R. A., Guerrero, M. A., et al. 2009, AJ, 138, 691
Ciardullo, R., Bond, H. E., Sipior, M. S., et al. 1999, AJ, 118, 488
Debes, J. H., Hoard, D. W., Kilic, M., et al. 2011, ApJ, 729, 4
Debes, J. H., & Sigurdsson, S. 2002, ApJ, 572, 556
de Marco, O. 2009, PASP, 121, 316
de Ruyter, S., van Winckel, H., Maas, T., et al. 2006, A&A, 448, 641
Diolaiti, E., Bendinelli, O., Bonaccini, D., et al. 2000, A&AS, 147, 335
Dole, H., Rieke, G. H., Lagache, G., et al. 2004, ApJS, 154, 93
Dong, R., Wang, Y., Lin, D. N. C., & Liu, X.-W. 2010, ApJ, 715, 1036
Dreizler, S., & Werner, K. 1996, A&A, 314, 217
Eisenstein, D. J., Liebert, J., Harris, H. C., et al. 2006, ApJS, 167, 40
Engelbracht, C. W., Blaylock, M., Su, K. Y. L., et al. 2007, PASP, 119, 994
Farihi, J., Jura, M., Lee, J.-E., & Zuckerman, B. 2010, ApJ, 714, 1386
Fazio, G. G., Hora, J. L., Allen, L. E., et al. 2004, ApJS, 154, 10
Fulbright, M. S., & Liebert, J. 1993, ApJ, 410, 275
Gordon, K. D., Engelbracht, C. W., Fadda, D., et al. 2007, PASP, 119, 1019
Gordon, K. D., Rieke, G. H., Engelbracht, C. W., et al. 2005, PASP, 117, 503
Harris, H. C., Dahn, C. C., Canzian, B., et al. 2007, AJ, 133, 631
Homeier, D., Koester, D., Hagen, H.-J., et al. 1998, A&A, 338, 563
Houck, J. R., Roellig, T. L., van Cleve, J., et al. 2004, ApJS, 154, 18
Jura, M. 2003, ApJ, 584, L91
Jura, M., Farihi, J., & Zuckerman, B. 2007, ApJ, 663, 1285
Kilic, M., & Redfield, S. 2007, ApJ, 660, 641
Kilic, M., von Hippel, T., Leggett, S. K., & Winget, D. E. 2005, ApJ, 632, L115
Kilic, M., von Hippel, T., Leggett, S. K., & Winget, D. E. 2006, ApJ, 646, 474
Krist, J. E. 2006, Spitzer Tiny TIM User's Guide Version 2.0, http://ssc.spitzer.caltech.edu/mips/psf.html
Kwitter, K. B., & Jacoby, G. H. 1989, AJ, 98, 2159
Liebert, J., Bergeron, P., & Holberg, J. B. 2005, VizieR Online Data Catalog, 215, 60047
Liebert, J., Green, R., Bond, H. E., et al. 1989, ApJ, 346, 251
McCook, G. P., & Sion, E. M. 1999, ApJS, 121, 1
Mullally, F., Kilic, M., Reach, W. T., et al. 2007, ApJS, 171, 206
Napiwotzki, R. 1999, A&A, 350, 101
Napiwotzki, R. 2001, A&A, 367, 973
Napiwotzki, R., & Schönberner, D. 1995, A&A, 301, 545
Nordhaus, J., & Blackman, E. G. 2006, MNRAS, 370, 2004
Phillips, J. P. 2003, MNRAS, 344, 501
Phillips, J. P. 2004, MNRAS, 353, 589
Rauch, T., Koeppen, J., & Werner, K. 1996, A&A, 310, 613
Rauch, T., Köppen, J., Napiwotzki, R., & Werner, K. 1999, A&A, 347, 169
Rauch, T., Werner, K., Ziegler, M., et al. 2009, in AIP Conf. Proc. 1135, Future Directions in Ultraviolet Spectroscopy, ed. M. E. V. Steenberg, G. Sonneborn, H. W. Moos, & W. P. Blair (Melville, NY: AIP), 171
Reach, W. T., Kuchner, M. J., von Hippel, T., et al. 2005, ApJ, 635, L161
Rieke, G. H., Su, K. Y. L., Stansberry, J. A., et al. 2005, ApJ, 620, 1010
Rieke, G. H., Young, E. T., Engelbracht, C. W., et al. 2004, ApJS, 154, 25
Skrutskie, M. F., Cutri, R. M., Stiening, R., et al. 2006, AJ, 131, 1163
Smith, J. D. T., Armus, L., Dale, D. A., et al. 2007, PASP, 119, 1133
Soker, N. 1998, ApJ, 496, 833
Su, K. Y. L., Chu, Y.-H., Rieke, G. H., et al. 2007, ApJ, 657, L41
Su, K. Y. L., Rieke, G. H., Stansberry, J. A., et al. 2006, ApJ, 653, 675
Taam, R. E., & Ricker, P. M. 2010, New Astron. Rev., 54, 65
Trilling, D. E., Bryden, G., Beichman, C. A., et al. 2008, ApJ, 674, 1086
Tylenda, R., Acker, A., Stenholm, B., & Koeppen, J. 1992, A&AS, 95, 337
von Hippel, T., Kuchner, M. J., Kilic, M., Mullally, F., & Reach, W. T. 2007, ApJ, 662, 544
Werner, K., Bagschik, K., Rauch, T., & Napiwotzki, R. 1997, A&A, 327, 721
Werner, M. W., Roellig, T. L., Low, F. J., et al. 2004, ApJS, 154, 1
Wesemael, F., Green, R. F., & Liebert, J. 1985, ApJS, 58, 379
Wyatt, M. C. 2008, ARA&A, 46, 339
Zuckerman, B., & Becklin, E. E. 1987, Nature, 330, 138
Zuckerman, B., Koester, D., Melis, C., Hansen, B. M., & Jura, M. 2007, ApJ, 671, 872